Advanced Composites and Hybrid Materials (2024) 7:183
https://doi.org/10.1007/s42114-024-01013-2

RESEARCH

Computational fluid-particle dynamic model guiding bioengineered magnetic nanomedicine for personalized brain-targeted drug delivery

Nguyen Nguyen[1] · **Muzhaozi Yuan**[1] · **Hanwen Hu**[1] · **Zhifeng Xiao**[3] · **Tianzhu Fan**[1] · **Tian-Hao Yan**[3] · **Ying Li**[1] · **Hong-Cai Zhou**[3] · **Jean-Philippe Pellois**[2] · **Ya Wang**[1,4,5]

Received: 18 April 2024 / Revised: 19 July 2024 / Accepted: 9 October 2024

Abstract

Neurodegenerative diseases pose significant challenges to global healthcare, exacerbated by complexities of the central nervous system and blood–brain barrier. While FDA-approved magnetic nanocarriers offer promising solutions for targeted drug delivery, inherent challenges in predicting delivery performance still hinder clinical practice. Existing brain vasculature transport models often lack accuracy in the 3D construction of the brain vasculature network and physiology of blood circulation, limiting progress in targeted drug delivery. This paper introduced the Circle of Willis's novel computational fluid dynamics framework to address these challenges. Utilizing patient-specific vascular geometries and incorporating complexities of blood circulation, hemodynamics, and the rheology for non-Newtonian fluid effect, our approach provides unprecedented insights into drug carrier dynamics in the mouse brain vasculature. Furthermore, we performed a comparative study simulating the dynamic transport using three types of magnetic nanocarriers—gold-coated superparamagnetic iron oxide (Au-SPIO), hollow-gold nano-shell enclosed superparamagnetic iron oxide (HGNS-SPIO), and metal–organic frameworks loaded with iron oxide (MOF-Fe_3O_4)—to predict their transport in adult mice's brain under magnetic targeting. The simulation was validated by in vivo results by comparing the bioavailability of nanoparticles in different brain regions. Under a non-magnetic field, simulations revealed a capture efficiency of around 10.5% for all three types of nanoparticles, with size-dependent patterns favoring smaller sizes. With the presence of a magnetic field, MOF-Fe3O4 demonstrated the highest capture efficiency with "single magnet" at 11.19%, while Au-SPIO in "linear Halbach array" and MOF-Fe_3O_4 in "circular Halbach array" layouts reached 10.9%. Finally, we demonstrated high biocompatibility for all three nanocarriers, with no toxicity for Au-SPIO and MOF-Fe_3O_4 at 40 µg/mL and for HGNS-SPIO at 20 µg/mL. Effective cell uptake was also observed for all three nanocarriers. This comprehensive study addresses critical knowledge gaps, providing insights into the dynamics of magnetic nanocarrier transport within the brain and paving the way for highly effective, personalized therapies for neurological disorders.

Keywords Brain-specific drug delivery · Neurodegenerative disease · Magnetic nanoparticles · Computational-fluid dynamic · Circle of Willis · Magnetic application

---

✉ Nguyen Nguyen
nnguyen18@tamu.edu

✉ Ya Wang
ya.wang@tamu.edu

[1] J. Mike Walker '66 Department of Mechanical Engineering, Texas A&M University, College Station, TX 77840, USA

[2] Department of Biochemistry and Biophysics, Texas A&M University, College Station, TX 77843, USA

[3] Department of Chemistry, Texas A&M University, College Station, TX 77843, USA

[4] Department of Biomedical Engineering, Texas A&M University, College Station, TX 77843, USA

[5] Department of Electrical and Computer Engineering, Texas A&M University, College Station, TX 77843, USA

1 Introduction

Neurological disorders, impacting around 15% of the global population [1], stand as the primary contributors to both physical and cognitive disabilities on a worldwide scale. Within this spectrum, neurodegenerative diseases, such as Alzheimer's disease (AD), Parkinson's disease (PD), and Huntington's disease, cast a profound impact on patients' conditions in various aspects of the well-being of individuals, influencing diverse facets of their conditions. From memory and motor function impairment to emotional and behavioral alterations, these diseases present intricate challenges that extend beyond the individual, affecting families, caregivers, and societies at large. Considerable resources have been invested in pursuing novel and effective therapeutic strategies for these diseases. Recent studies have highlighted significant advancements in drug bioavailability and applicability through innovative nanoparticle formulations, such as magnetic nanoparticles, liposomes, and hydrogels as well as targeted delivery systems like microneedles and transdermal patches [2, 3]. Innovations in materials science, such as metal–organic frameworks and hybrid nanocarriers, have shown great promise in achieving controlled, sustained drug release [4, 5]. However, the quest for efficient, targeted drug delivery approaches for brain-specific diseases within the intricate environment of the brain remains a compelling challenge.

Precise drug targeting within the central nervous system (CNS) is crucial for treating neurological conditions. The path of therapeutics from the point of administration to the neural tissue is laden with hurdles, such as navigating the complex vascular system and breaching the formidable blood–brain barrier (BBB) [6]. For most conventional administration methods, the accumulation of medicines at the designated site is directly associated with their blood circulation. Longer exposure time ensures a higher chance of drug retention and the availability of drugs at the target site [7]. This is highly patient-specific due to differences in geometrical features of the individual's vasculature network that could affect the outcome of therapeutic intervention.

Furthermore, drugs that reach the brain via the blood compartment must also pass the BBB, a network of endothelial cells that prevents external molecules from internalizing into the brain. The intensively selective BBB rejects over 98% of the small molecules exceeding a specific size, significantly limiting their ability to reach the brain and achieve effective dosage [8]. Precision nanomedicine has emerged as a promising avenue, offering the potential for targeted and tailored drug delivery. Numerous studies have explored the application of nanocarriers for brain drug delivery, with magnetic nanoparticles (MNPs) garnering significant attention [9–11]. These MNPs respond to magnetic fields, enabling navigation in the bloodstream and selective breach of the BBB. The flexibility in size, morphology, and chemical functionality has served different advantages of MNPs in vivo [12, 13]. Their tunability and diverse composition not only ensure high biocompatibility but also provide high stability under physiological conditions.

Recent advancements in magnetic nanomaterials have significantly enhanced its ability to be guided by external magnetic fields, higher loading rate, and functionalization. For instance, novel magnetic nanocomposites have been developed that integrate chitosan to improve the magnetic nanoparticle's environmental friendliness and adsorption capacity [14]. Considering the findings of Kim et al., silica-overcoated MNPs expressed no apparent toxicity in mice after intraperitoneal injection after 4 weeks [15]. These MNPs were also detected in the brain, indicating their penetration capability across BBB. Nevertheless, the dynamic interaction between drug carriers and the biological system is left unchecked in the bloodstream post-injection, potentially resulting in a deviation from the intended drug delivery path. Currently, a method to accurately measure the delivery efficiency of various MNPs with targeted regions of the brains is starkly lacking. Experimentally investigating these phenomena in vivo poses considerable challenges, given the small size of drug molecules, the dynamic nature of the delivery process, and the complex vascular network [16]. Thus, developing a computational fluid-particle dynamic (CFD) model for transporting concentrated species inside the body is highly desirable as a practical numerical tool for drug development's decision-making system. Implementing this tool could save companies millions of dollars currently expended on animal testing and trial-and-error methods with research and development. Additionally, it could also significantly accelerate progress in clinical experiments. By offering a more humane, non-invasive, rapid, highly precise, and cost-effective avenue, this transformative approach holds many potential benefits for the development of drug delivery.

Currently, the integration of CFD simulation for understanding MNP dynamic transport within the brain vasculature is in the developing phase. Nevertheless, it is quickly becoming a focal point in precision nanomedicine. This burgeoning approach holds immense promise for advancing the development of a more dependable drug delivery system. By offering a virtual platform to model and analyze the intricate fluid dynamics involved in MNP transport, these simulations pave the way for a nuanced comprehension of the variables influencing drug delivery to the brain. Several attempts have been made to study the delivery of MNPs inside the brain's vasculature. Lunnoo and Puangmali presented a 2D theoretical study of blood flow with spherical MNPs, including Fe, Fe_3O_4, and Fe_2O_3, intra-arterially injected through a human capillary when exposed to an alternating magnetic field. They investigated the MNPs with sizes ranging from 10 nm to 4 µm. Their study utilized a continuum-based model to simulate the blood flow and magnetic nanoparticle dynamics, proving the effects of size, concentration, and magnetic properties on the localization and distribution of MNPs within the domain over time [17].

Similarly, Kosari and Vafai introduced a two-dimensional theoretical study of a blood flow carrying spherical Fe_3O_4 MNPs (10–22 nm) inside brain microvascular vessels to study the transport and thermal effects of MNPs in cerebral blood circulation [18]. Their model employed a discrete-phase model to simulate nanofluidic dynamics by solving the Navier–Stokes equations coupled with the energy equation. The results demonstrated that a computational model could predict the impact of MNP injection on the capillary to benefit conventional therapy. However, these methods employed a 2D representation, often oversimplifying the three-dimensional geometry and physiology of the brain vessels, potentially leading to MNP transport dynamics that deviate significantly from reality. The transition from 2 to 3D simulations represents a significant leap forward in the quest for a more dependable drug delivery system by modeling a whole human's Circle of Willis (CoW) or natural vessel from the brain [19, 20]. However, these models still represent a simplified version of brain vasculature by modeling an ideal symmetrical geometry for the CoW, with idealized branching structures and a constant cylindrical profile inside the blood vessel. As a result, geometry would not capture the intricate reality within the brain's vasculature or the personalized nuances of each individual's vascular network. Patient-specific geometry is so paramount as it acknowledges the inherent variability in anatomical structures, including variations in vessel shapes, sizes, branching patterns, and curvature, among individuals. This anatomical realism is essential for accurately representing blood flow dynamics within the intricate network of the brain's vasculature. Significantly, few studies have utilized patient-specific data to model the transport process inside the brain vasculature due to the lack of experimental resources and interdisciplinary collaboration. Kenjeres and Righold simulated the blood flow and magnetic drug carrier distributions in a complex brain vascular system based on human patients' magnetic resonance imaging (MRI) scan images [21]. Their carrier MNPs mimicked the medical drug epirubicin by modeling them as double-layer magnetic-core spherical nanoparticles with diameters ranging from 0.25 to 4 µm. They applied a finite element method to solve the coupled fluid-particle interaction equations under steady-state conditions.

A more recent study by Chen and Wang attempted to address the same issue by developing an analytical model of finite element model describing the personalized dynamic transport of Fe_3O_4 spherical magnetic nanorobots (40 nm) inside a real brain vasculature [22]. Both studies designed the optimal transport path based on the reconstructed vascular model from actual patients, introducing a more realistic representation of localized, non-invasive treatment for the brain. Nevertheless, these two models assumed a steady boundary condition, ignoring the time-dependency of blood flow due to heartbeats and blood pressure. Meanwhile, they also neglected blood rheology complexities like viscosity and pulsatile flow in the blood flow simulation, like other traditional CFD simulations [23–25]. The fluid properties of the model serve as an underlying framework for enhancing the accuracy and realism of simulations. Consequently, the current state of the art for drug delivery necessitates a more sophisticated representation to address all these issues.

Against this backdrop, our research proposes a model of MNP transport using a 3D accurate geometry reconstruction model for the adult mouse brain's CoW. This advanced model accurately represents realistic vascular anatomy within the brain by incorporating patient-specific branching patterns, vessel diameters, and spatial arrangement using MRI data. Built upon this framework, our MNP transport model takes a significant leap forward in capturing the complexities of blood circulation by accounting for the curvature, pressure distribution, and shear stress tailored to the patient's specific brain environment. Our study captures blood's unique rheological and hemodynamic properties more accurately by considering non-Newtonian behaviors, variations in blood viscosity, and actual pulsatile flow patterns. This approach not only refines the precision of our simulations to in vivo study but also enhances our findings' overall reliability and relevance, setting a new standard in the investigation of MNP behavior within the central nervous system. We tested our model on three different functionalized iron oxide MNPs: gold-coated superparamagnetic iron oxide (Au-SPIO) NPs, hollow gold nano-shell-coated superparamagnetic iron oxide (HGNS-SPIO) NPs, and metal–organic frameworks (MOF) loaded with Fe_3O_4 (MOF-Fe_3O_4) NPs to study the transport dynamics of different carriers in the mouse brain under magnetic targeting effects. The selection of the three different functionalized magnetic nanoparticles—Au-SPIO, HGNS-SPIO, and MOF-Fe3O4—was strategically aimed at leveraging their unique and complementary properties for brain-targeting drug delivery applications. Au-SPIO NPs were chosen for their small size, strong magnetic properties, and enhanced biocompatibility and stability due to the gold coating, aiming for better targeting efficiency. HGNS-SPIO NPs, with their gold-coated surface, offer good biocompatibility and enhanced drug-loading capacity due to their hollow structure, although they have weaker magnetic properties compared to Au-SPIO. MOF-Fe3O4 NPs, being the largest, provide high surface area and porosity for significant drug loading and controlled release, combined with the strong magnetic properties of Fe3O4 for magnetic targeting. Together, these MNPs provide a versatile platform for our research, exploiting their individual and synergistic benefits to potentially lead to more effective solutions in nanomedicine. The bioavailability of each type of MNP is evaluated in the midbrain, cerebellum, and cortex regions to compare with in vivo outcomes and validate the model. Furthermore, we also investigate the interaction of different nanocarriers with the biological environment to serve as a comparative study that meticulously assesses the potential of various MNPs for brain-specific drug delivery purposes. This investigation strongly emphasizes a comprehensive evaluation of MNP transport inside the brain vasculature while considering other vital aspects, such as cytotoxicity and cellular uptake rates, for realistic application.

By systematically evaluating the performance of these promising bioengineered MNPs made of FDA-approved materials, our study addresses the current knowledge gaps by providing a more robust understanding of MNPs transport in the brain that can significantly reduce the time, effort, and financial resources required for drug development. This work could expedite the drug design process, ushering in more efficient and cost-effective approaches for treating neurological disorders.

2 Material preparation

2.1 Preparation of Au-SPIO NPs

The Au-SPIO NPs were synthesized following a documented protocol [26]. Initially, a 2 mL solution of 4.66 mM SPIO (Ferrotec EMG 304) was stirred with 6 mL of 0.1 M sodium citrate ($C_6H_5Na_3O_7$) for 10 min to facilitate OH^- to citrate anion exchange. After dilution to 100 mL with deionized (DI) water, 0.5 mL of 1% $HAuCl_4$ was added, and the pH was adjusted to 9–10 using 0.1 M NaOH. Subsequently, 0.6 mL of 0.2 M $NH_2OH{\cdot}HCl$ induced the initial gold coating, turning the solution from brown to purple.

To increase gold coating thickness, 0.5 mL of 1% $HAuCl_4$ and 0.2 mL of 0.2 M $NH_2OH{\cdot}HCl$ were sequentially added. This process was repeated until the solution turned red, indicating the final coating thickness. All chemicals were sourced from Sigma-Aldrich (St. Louis, MO), ensuring the reliability of the synthesis for diverse research applications.

2.2 Preparation of HGNS-SPIO NPs

The synthesis commenced with preparing SPIO core NPs using a straightforward co-precipitation method. Initially, a solution containing 2 mmol of $FeCl_3$, 1 mmol of $FeSO_4$, and 0.1 mmol of sodium dodecyl sulfate (SDS) dissolved in 200 mL of DI water was created. Subsequently, 80 mL of 125 mM NaOH solution was gradually added at room temperature. Upon turning black, the solution was centrifugated and washed with DI water and ethanol multiple times. The resulting precipitate (Fe_3O_4) was magnetically collected, suspended in 80 mL of DI water, and stored in a refrigerator.

The next step involved oxidizing Fe_3O_4 to magnetic γ-Fe_2O_3. For this, 20 mL of the Fe_3O_4 suspension was diluted to 100 mL with DI water, and 0.1 mL of concentrated HNO_3 (70%) was added. The mixture was heated at 90 °C in an oil bath for 30 min, transforming its color from black to brown, indicating the oxidation process. After centrifugation and washing with DI water, the resulting precipitate (γ-Fe_2O_3) was preserved in 20 mL of DI water, constituting the SPIO suspension. Ag-SPIO NPs were then crafted as templates. In this step, 0.5 mL of the SPIO suspension and 1 mL of 30 mM trisodium citrate were added to 17 mL of DI water. The solution was heated at 60 °C in an oil bath for 10 min, then slowly adding 2 mL of 20 mM $AgNO_3$. After an additional 10 min, 5 mL of 5 mM NaOH was gradually introduced to facilitate the precipitation of Ag^+ on the γ-Fe_2O_3 surface. The heating process continued for 210 min, resulting in a brownish-yellow appearance and indicating the formation of an Ag-SPIO suspension.

Finally, for the synthesis of HGNS-SPIO NPs, 0.53 mL of 25 mM $HAuCl_4$ was slowly added to the Ag-SPIO suspension at 60 °C, initiating the replacement of Ag^+ by Au^{3+}. The heating process for this displacement reaction persisted for another 30 min, leading to the collection of a blue-colored product, denoted as the HGNS-SPIO suspension.

2.3 Preparation of MOF-Fe_3O_4 NPs

The MOF-Fe_3O_4 NPs were synthesized following a documented protocol [27] with slight modification. The carboxyl functionalized Fe_3O_4 particles were synthesized via a solvothermal method. In brief, $FeCl_3{\cdot}6H_2O$ (1.6 g), NH_4OAc (4.0 g), and EDTA-2Na (1 g) were dissolved in ethylene glycol (100 mL) and stirred for 2 h at 50 °C. The solution was then transferred to a Teflon-lined stainless-steel autoclave and maintained at 200 °C for 12 h. After cooling, magnetite precipitates were separated by magnetic separation, washed with anhydrous ethanol and DI water, and vacuum-dried at 60 °C for 24 h.

The core–shell structured MOF-Fe_3O_4 composites were prepared through a stepwise self-assembly procedure with previous magnetite particles as cores. Specifically, 0.1 g of carboxyl functionalized Fe_3O_4 NPs was dispersed in an ethanol solution of $FeCl_3{\cdot}6H_2O$ (10 mL, 10 mM) under ultrasonication. Subsequently, an H_3BTC ethanol solution (10 mL, 10 mM) was added and stirred at 70 °C for 2 h. The solid product was collected using a permanent magnet and washed with anhydrous ethanol, and the final Fe_3O_4@MIL-100(Fe) composite (named MOF-Fe_3O_4) was obtained after ten cycles of coating Fe_3O_4 cores with MIL-100(Fe), followed by overnight drying at 60 °C.

2.4 Characterization

We employed transmission electron microscopy (TEM) to evaluate the morphological characteristics and determine the size distribution of the MNPs. Specifically, the detailed structure and morphology were scrutinized using an FEI Tecnai G2 F20 ST field emission transmission electron microscope (FE-TEM) (FEI Company, USA) at an accelerating voltage of 200 kV. The size distribution analysis involved the measurement of a minimum of 100 NPs, with inner and outer diameters determined using ImageJ.

The light absorption spectra of the MNPs were recorded using a Hitachi U-4100 UV–Vis-NIR spectrophotometer (500–1200 nm) (Hitachi, Japan). For each measurement, 3 mL of NP solution was added to the cuvette. Additionally, the hydrodynamic diameters and zeta potential of the MNPs, both with and without functionalization, were assessed via dynamic light scattering (DLS) using a Zetasizer apparatus from Malvern Instruments (Malvern, UK). The hydrodynamic diameter was calculated through CONTIN analysis of the intensity-weighted distribution function embedded in the Malvern software.

The magnetic susceptibility was measured by determining the magnetic hysteresis curve with a vibrating sample magnetometer (VSM) of Quantum Design MPMS-XL SQUID (Quantum Design, USA) in the field range from − 30 to + 30 kOe. For accuracy, all measurements were conducted in triplicates.

3 CFD simulation

3.1 Geometry reconstruction

To analyze blood flow dynamics and motion of MNPs inside the mouse brain, we used the CoW junction to investigate the transport of MNPs entering the brain due to its role as the main blood supply to the CNS. The CoW is situated at the base of the brain, where the brainstem connects to the brain, and plays a pivotal role in cerebral circulation. It is formed by the joining of several major arteries in the cerebral hemispheres: internal carotid arteries (ICAs), vertebral arteries (VAs), posterior cerebral arteries (PCAs), superior cerebellar arteries (SCAs), anterior and middle cerebral arteries (ACAs and MCAs). These arteries contribute to and maintain adequate perfusion to various brain regions.

Figure 1 depicts the modeling methodology for reconstructing the CoW geometry from images to the final CAD model in SolidWorks—the raw MRI data obtained from reference [28] represented the realistic CoW geometry of an 8-week-old male C57BL/6 mouse. The quality of the raw imaging data from MRI was improved by color inverting and an image segmentation process using Otsu’s method to separate the CoW from the background [29]. The images were imported into SolidWorks to reconstruct the CAD model and eventually refine the volumetric structure.

3.2 Dynamic model of MNP transport

3.2.1 Fluid phase (blood)

This study conceptualized blood as a continuous non-Newtonian fluid, adopting a model that assumes laminar, pulsatile, and incompressible flow based on prior research [19, 30]. The specific blood density for C57BL/6 mice is not readily available in the literature. However, the density of other types of mice and rat blood similar to our subject was close to 1060 kg/m^3, confirming it is the typical blood density for mice [31, 32]. The blood viscosity was modeled using the Carreau-Yasuda model [33]. Given the low volume fraction of the discrete phase, the influence of MNPs on the base fluid was deemed negligible, warranting consideration as one-way coupling exclusively. The continuity and momentum equations are expressed as follows [19]:

$$\nabla . u_f = 0 \tag{1}$$

$$\rho\left(\frac{\delta u}{\delta t} + \left(u_f . \nabla\right) u_f\right) = -\nabla p + \mu \nabla^2 u_f \tag{2}$$

Here, u_f represents the fluid velocity vector, ρ signifies the density of blood, p denotes pressure, and μ represents dynamic viscosity.

The non-Newtonian nature of blood rheology, acknowledged for the significance of shear rate on viscosity, is described by the Carreau-Yasuda model [33]:

$$\mu(\dot{\gamma}) = \mu_\infty + \left(\mu_0 - \mu_\infty\right)\left(1 + (\lambda\dot{\gamma})^2\right)^{\frac{n-1}{2}} \tag{3}$$

In the above relation, $\dot{\gamma}$ is the strain rate, μ_∞ is the infinite shear rate viscosity, μ_0 is the zero-shear rate viscosity, λ is the relaxation time, and n is the power index. The values of the parameters mentioned in this work (Table 1) are obtained from the literature [34] for the same C57BL/6 mice type at a hematocrit level of 0.4, with consideration of the close age range to the model subject. These parameters were later input into COMSOL Multiphysics for the Laminar Flow Module to compute the fluid flow field of blood.

3.2.2 Particle phase (MNPs)

For the discrete phase, MNPs were modeled as point-like entities, neglecting their individual volume and assuming

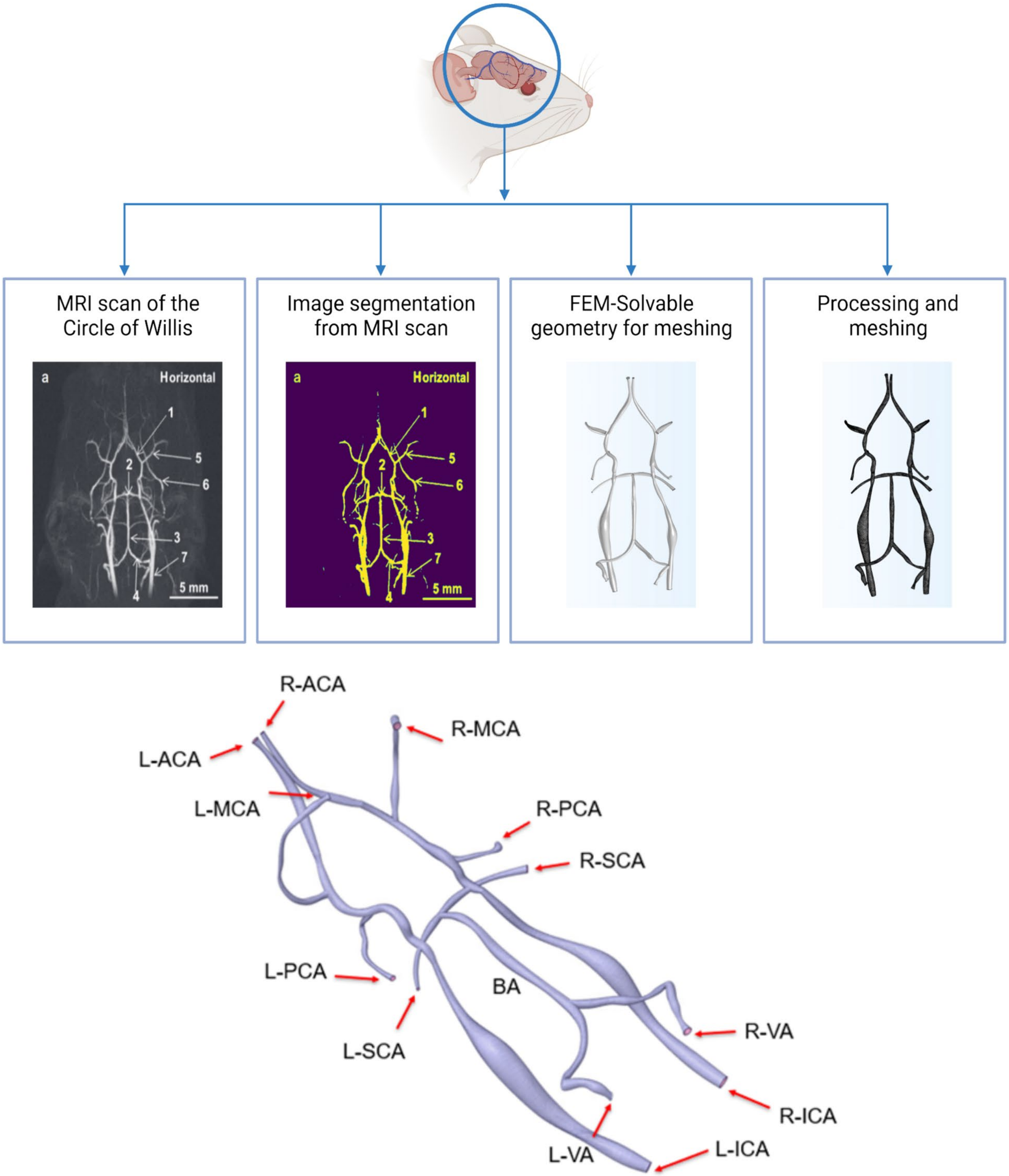

Fig. 1 The steps of preparing the reconstruction of the CoW and final geometry for the simulation

a uniform spherical shape within the blood flow. Inside the CoW, the movement of MNPs is influenced by various factors stemming from fluid dynamics, boundaries, and external forces. These forces encompass viscous drag force, MNP-fluid interaction force, interparticle force, gravitational force, Brownian force, and forces arising from magnetic or electrical fields [35]. Nonetheless, to minimize computational complexity and allow efficient simulation of particle dynamics over time, we only consider MNPs at low concentration. Drawing from the insights provided in [19] and

Table 1 Parameters of blood and vessel for simulating the transport of MNPs

Parameter	Symbol	Default value
Hematocrit[a]	Hct	0.4
Infinite shear rate viscosity[a]	μ_∞	0.003 (kg/m.s)
Zero-shear rate viscosity[a]	μ_0	0.223 (kg/m.s)
Power index[a]	n	0.555
Relaxation time[a]	λ	− 174.994
Blood density[b]	ρ	1060 (kg/m^3)
Left ICA diameter[c]	d_{L-ICA}	0.183 (mm)
Right ICA diameter[c]	d_{R-ICA}	0.158 (mm)
Left VA diameter[c]	d_{L-VA}	0.119 (mm)
Right VA diameter[c]	d_{R-VA}	0.126 (mm)

[a] Value obtained from the literature [34]

[b] Value obtained from the literature [32]

[c] Value obtained from the geometry model of COMSOL

taking into account the size of the mouse brain, we adopt a continuous release strategy of 20 MNPs per 0.02 s from $t=0$ s to $t=0.8$ s (total of 3200 MNPs) of each type (Au-SPIO, HGNS-SPIO, and MOF-Fe$_3$O$_4$) through the four inlet boundaries. This frequency injection is not meant to reflect clinical practice but to provide a granular understanding of MNPs in a controlled, time-resolved manner. Administering nanoparticles at such a steady frequency is impractical due to limitations like half-life, metabolism, and clearance mechanisms. Our approach uses continuous injection as a computational technique to mimic the overall effect of periodic clinical doses, allowing us to capture detailed nanoparticle distribution dynamics and infer behavior over realistic dosing schedules. The interaction between the MNPs and the blood was addressed through one-way coupling and assuming no interparticle effects, acknowledging the negligible impact of the MNPs on the base fluid as well as among each other.

Due to the small size of the MNPs, drag force (F_f), magnetic force (F_{mag}), and Brownian force ($F_{Brownian}$) appear as dominant forces, while other forces are neglected due to insignificant effects. However, the consideration of MNP diffusion due to Brownian motion is contingent upon the MNP diameter being sufficiently small; a threshold can be estimated using the following criterion [35]:

$$|F|D_p \le kT \tag{4}$$

where $|F|$ is the magnitude of the total applied force acting on the MNP, D_p is the MNP diameter threshold, T is the absolute temperature (measured in Kelvin), and k is the Boltzmann's constant. This criterion suggests that Brownian motion becomes significant when the energy exerted by the applied force in moving the MNP at a distance equal to its diameter is less than or comparable to thermal energy kT. Depending on the MNP's intrinsic hydrodynamic and magnetic properties, the threshold diameter varies across different materials. Gerber et al. have studied the threshold for various materials and estimated the critical particle diameter to be 40 nm with $|F| = 0.1$ pN for Fe$_3$O$_4$, 200 nm for α-Fe$_2$O$_3$ with $|F| = 0.02$ pN, 600 nm for Au with $|F| = 0.0067$ pN, and so forth [36]. For particles with a diameter larger than the critical diameter, we could use the Newtonian equation for the trajectory of a single particle. By leveraging the results from the COMSOL simulation, we can derive the total force absolute value $|F|$ acting on the particles from the software. Subsequently, we can use Eq. 4 to approximate the threshold diameter D_p for all three types of MNPs. As a result, the critical diameters for Au-SPIO, HGNS-SPIO, and MOF-Fe$_3$O$_4$ are approximately 14 nm, 44 nm, and 112 nm, respectively. All fall way below the hydrodynamic diameter obtained from our experimental findings. Thus, Brownian motion can be safely disregarded in our analysis, and we can use classical Newtonian physics to predict the motion of MNPs.

Table 2 Parameters of MNPs used for the simulation

	Au-SPIO	HGNS-SPIO	MOF-Fe$_3$O$_4$
Density	16,067 (kg/m^3)	10,415 (kg/m^3)	1775 (kg/m^3)
Susceptibility	25,898	2079	10,365

Eventually, the initial velocity of MNPs was assumed to be the same as the base fluid velocity. Drag force (F_f) acting on the MNPs was then modeled using relevant equations, such as the Stokes drag law for low Reynolds number flows [35]:

$$F_f = -6\pi\mu R_p(u_p - u_f) \tag{5}$$

where R_p and u_p are the MNP's hydrodynamic radius and velocity, respectively.

The magnetic force (F_{mag}) acts on MNPs in the presence of an external magnetic field (B) can be expressed as [37]

$$F_{mag} = \mu_f\left(m_{p,eff}.\nabla\right)H_a \tag{6}$$

where μ_f is the permeability of the blood and H_a is the external magnetic field strength. $m_{p,eff}$ represents the effective dipole moment of the MNPs and is defined as [37]

$$m_{p,eff} = V_p\frac{3\left(\chi_p - \chi_f\right)}{\left(\chi_p - \chi_f\right) + 3\left(\chi_f + 1\right)}H_a \tag{7}$$

where V_p is the volume of a single MNP and χ_p and χ_f are the susceptibility of the MNPs (indicated for each type in Table 2) and the fluid, respectively. When $\left|\chi_f\right| \ll 1(\mu_f \approx \mu_0)$, the magnetic force becomes

$$F_{mag} = \mu_0 V_p \frac{3(\chi_p - \chi_f)}{(\chi_p - \chi_f) + 3(\chi_f + 1)} (H_a . \nabla) H_a \quad (8)$$

The motion of MNPs is described by Newton's second law from trajectory as follows [35]:

$$m_p \frac{du_p}{dt} = \sum F = F_m - F_f \quad (9)$$

where m_p and u_p are the mass and velocity of the MNPs and drag force (F_f) and magnetic force (F_{mag}) representing the sum of all external forces. The inertial term $m_p \frac{du_p}{dt}$ is ignored for submicron particles since their mass is negligible. The above equation becomes as follows:

$$F_{mag} - F_f = 0 \rightarrow u_p = u_f + \frac{F_{mag}}{6\pi \mu R_p} \quad (10)$$

3.2.3 Capture efficiency

Braak's theory proposes a staging system for PD progression, suggesting an ascending pattern of affected brain areas according to different stages [38]. Starting with stages 1 and 2, PD begins in the olfactory bulb and lower brainstem regions. These areas affected can be accessed through the bloodstream provided by PCAs and SCAs. Progressing to stages 3 and 4, the pathology extends to the midbrain, particularly affecting the substantia nigra with motor symptoms, which is accessible via both MCAs and PCAs. Finally, in stages 5 and 6, the disease reaches the remote area of the cerebral cortex, leading to cognitive and behavioral impairments commonly observed in advanced PD. This region is only accessible through the ACAs, posing further challenges for drug delivery through the bloodstream. The schematic in Fig. 2 further illustrates the supply arteries corresponding to affected brain regions in detail. While Braak's theory specifically pertains to human brains, we adopt similar principles to study the same neurodegenerative diseases in mice models since we only focus on targeting different regions of drug carriers using magnetic field.

To quantify the capture efficiency of MNPs targeting these regions, measurements can be taken using the ratio of injected MNPs to those leaving the interest outlet region, facilitated by different configurations of magnetic fields using

$$\eta_{capture} = \frac{N_{np,in}}{N_{np,out}} \times 100\% \quad (11)$$

This approach enables researchers to assess the effectiveness of MNP-based drug delivery systems in targeting specific brain regions implicated in PD pathology, thereby increasing the robustness of therapeutic interventions.

3.2.4 Magnetic field

The magnetic field application played a pivotal role in influencing the trajectory of MNPs to the area of interest. For this simulation, a magnetic field generated by different configurations of cubic permanent neodymium magnet (NdFeB, grade 52) with 12.7 × 12.7 × 12.7 mm, as shown in Fig. 3, was modeled to manipulate MNP movement within the study. In Fig. 3, the arrows represent the magnetization direction of the magnets, flowing from the south pole (S) to the north pole (N) inside the magnet. The determination of the magnetic field utilizes Ampere and Gauss's law equations [39].

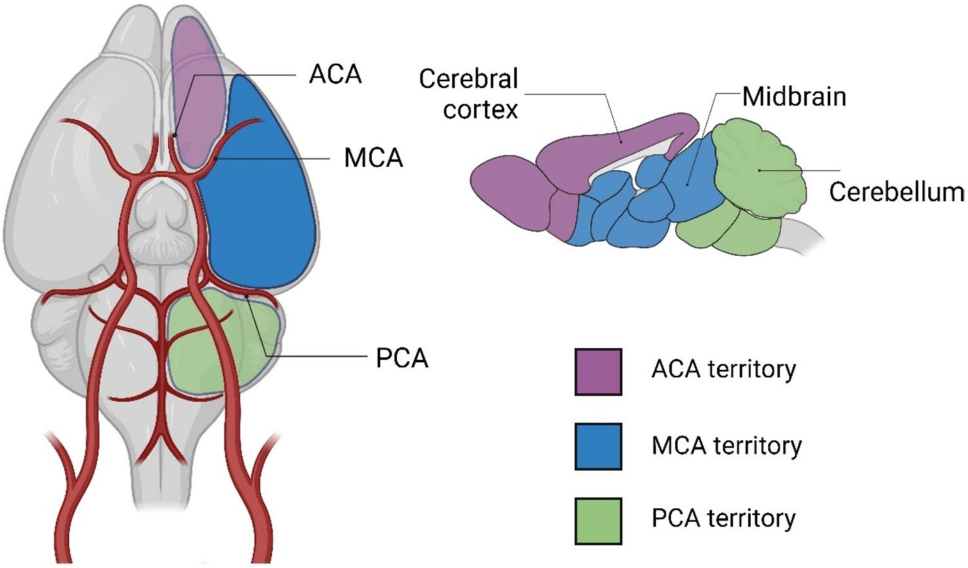

Fig. 2 Arterial supply to different brain regions from CoW

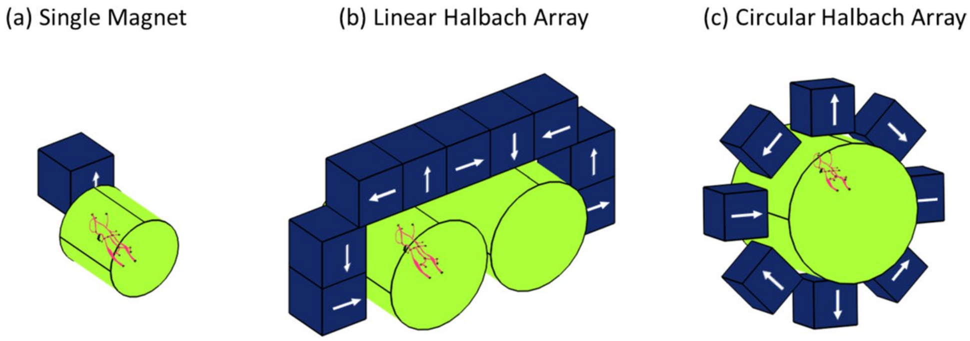

Fig. 3 Different magnetic applications for the brain targeting effect in the CoW with the mouse's head placed inside the cylindrical chamber. **a** Single magnet. **b** Linear Halbach array. **c** Circular Halbach array

Table 3 Parameters of magnetic application settings used for the simulation

Parameter	Symbol	Default value
Vacuum permeability	μ_0	$4\pi\times10^{-7}$ (H/m)
Blood permeability	μ_{blood}	0.99999
Remanent magnetic flux density	B_{rem}	1.48 (T)

$$\nabla \times H = 0 \tag{12}$$

$$\nabla . B = 0 \tag{13}$$

where H represents the magnetic field intensity (equal to zero due to no current) and B is the magnetic flux density.

For blood, the magnetization is zero in the environment. Hence, the stationary magnetic field encompassing the permanent magnet is derived from the subsequent equation [40].

$$B = \mu_0\mu_r H + B_{rem} \tag{14}$$

Here, μ_0 denotes the magnetic permeability of the vacuum, μ_r is the relative magnetic permeability of the surroundings, and B_{rem} is the permanent magnetic flux density (Table 3). The difference in the magnetic permeability of the MNPs and their surroundings results in the magnetization of MNPs upon exposure to the external magnetic field. Meanwhile, to adhere to the limited body exposure of magnetic to the subject, we chose $B_{rem} = 1.48(T)$ to reflect the magnetic effect in real life [41]. The magnetic field map is solved by "Magnetic Field, No Current Module" in COMSOL Multiphysics software. Finally, this result is imported into the "Particle Tracing Module" to calculate the effect of the magnetic field on particle trajectory.

3.3 Boundary conditions

As shown in Fig. 1, there are four inlets in the CoW junction, including left and right ICAs and VAs. The ICAs are further divided into the ACAs and MCAs, while the VAs converge into the basilar artery (BA), branching into the PCAs and SCAs. Together, these six arteries comprise pressure outlets for the blood flow inside CoW. We obtained the inlet flow velocity for ICA and VA from the literature of C57BL/6 adult mice's experimental data using a combination of Doppler ultrasound and MRI measurement methods [42, 43] reflecting the pulsatile nature of blood circulation accurately. Subsequently, we derived these data as an unsteady velocity waveform using Python, as shown in Fig. 4. The artery wall is assumed to be rigid with non-slip conditions applied.

3.4 Mesh and numerical method

To capture complex fluid dynamics and MNP transport, the flow domain was discretized into many tetrahedral cells using COMSOL Multiphysics, employing a robust meshing strategy with 0.6 mm as the maximum element size. The mesh resolution was carefully chosen to balance accuracy and computational efficiency, ensuring convergence and stability during simulation. The choice of tetrahedral cells facilitated the efficient representation of irregular geometries and allowed for increased mesh flexibility. The mesh refinement was particularly emphasized near vessel boundaries and regions of interest, ensuring accurate resolution of flow patterns and MNP trajectories. A mesh quality study was performed to ensure that poor element quality will not affect the outcomes by measuring skewness, as shown in Fig. 5.

The Laminar Flow Module, Magnetic Fields (No Currents Module), Particle Tracing for Fluid Flow Module, and Transport of Diluted Species Module in COMSOL Multiphysics were utilized to solve the partial differential equations governing fluid flow, magnetic field, and MNP dynamics inside the CoW.

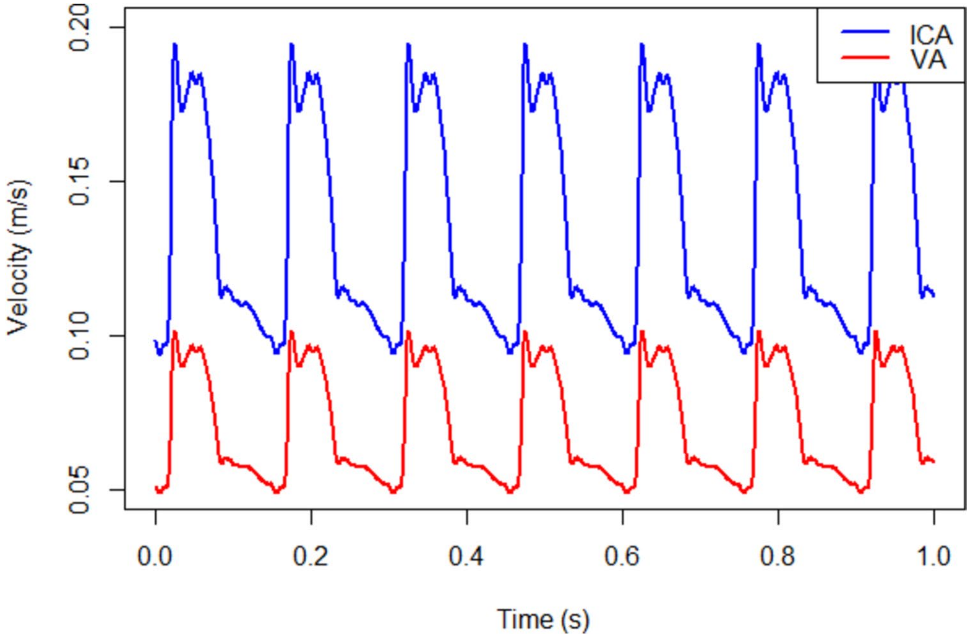

Fig. 4 An unstable physiological inlet velocity profile for ICAs and VAs was used in the simulation

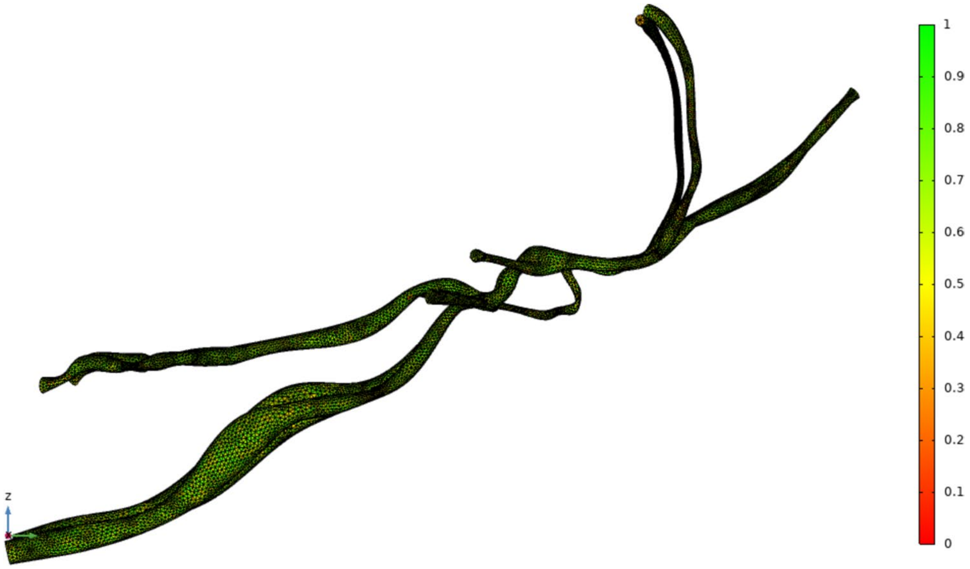

Fig. 5 Mesh quality of the geometry model (skewness)

4 In vitro study

4.1 Cell viability assessment

4.1.1 Neuro2a cell culture

The Neuro2a cell line, a murine neuroblastoma cell line commonly employed as an in vitro model for neurobiology research, was utilized in this study to assess the biocompatibility and cytotoxicity of various bioengineered MNPs for brain-specific drug delivery. The Neuro2a cell line (cat# CCL-131) was obtained from the American Type Culture Collection (Rockville, MD, USA). Cells were cultured in Dulbecco's Modified Eagle's Medium (DMEM) supplemented with 10% fetal bovine serum (FBS) and 1% penicillin–streptomycin antibiotic solution. The cells were maintained at 37 °C in a humidified atmosphere containing 5% CO2.

4.1.2 MNP treatment

Cells were seeded into 48-well tissue culture plates at a concentration of 2.2 cm^2/mL cells per well, which translates to approximately 29,920 cells per well. This seeding density guarantees optimal cell growth and uniform distribution for accurate cytotoxicity testing. After seeding, the cells were allowed to adhere and proliferate for 24 h to ensure they reached an optimal growth phase. Following the incubation period, the culture medium was aspirated from each well, and the cells were exposed to different bioengineered MNPs at various concentrations. The MNPs under investigation included Au-SPIO, HGNS-SPIO, and MOF-Fe_3O_4. The cells were treated with these MNPs for a designated period, typically 1, 2, and 3 days, to allow for MNP-cell interactions and potential internalization.

4.1.3 Cell viability assessment

Cell viability was assessed using flow cytometry. This method was chosen for its reliability and ability to measure quantitative cell viability. After the designated treatment period, the culture medium containing MNPs was removed, and the cells were washed with phosphate-buffered saline (PBS) to remove any residual MNPs. Subsequently, cells were detached, stained with SYTO 59 and SYTOX Green, and analyzed using a BD Accuri C6 Plus Flow Cytometer (BD, USA). The percentage of viable cells in each treatment group was determined based on the flow cytometry data.

4.2 Measurement of cell uptake rate

Similarly, to evaluate the cellular uptake of MNPs, Neuro2a cells were seeded into 48-well tissue culture plates at a concentration of 2.2 cm^2/mL cells per well. After 24 h of incubation to ensure adherence and growth, the cells were treated with Au-SPIO and HGNS-SPIO, respectively, for 2, 4, 8, and 12 h. Following treatment, cells were carefully detached using Trypsin–EDTA solution and collected into microcentrifuge tubes. The cellular uptake of MNPs was quantified using inductively coupled plasma mass spectrometry (ICP-MS). Before analysis, cells were digested using aqua regia (25% HNO_3, 75% HCl). ICP-MS then analyzed the resulting cell lysates to determine the gold concentration. ICP-MS data were then processed to calculate the amount of gold in treated cells, serving as a measure of MNP uptake. The results were expressed as nanograms of gold per cell and then converted to MNPs per cell to quantitatively assess cellular uptake.

4.3 Statistical analysis

All results were analyzed based on a minimum of three independent experiments and are expressed as mean values with standard deviations. Statistical analysis was conducted using the Mann–Whitney *U* test and one-way analysis of variance (ANOVA) followed by Tukey's post hoc test. Each nanoparticle-treated group was compared to the control group. A *p*-value of less than 0.05 was considered statistically significant.

5 Result and discussion

5.1 Characterization

The TEM images demonstrated the quasi-spherical morphology with uniform sizes of Au-SPIO, HGNS-SPIO, and MOF-Fe_3O_4 NPs (Fig. 6). While Au-SPIO exhibits a compact solid form, HGNS-SPIO and MOF-Fe_3O_4 showcase a core–shell structure comprising different iron oxide magnetic cores. Considering the heavier external gold coating of HGNS-SPIO which may compromise their magnetic properties, we used SPIO cores synthesized by the co-precipitation method, which has a larger diameter than the core of Au-SPIO. To further improve the magnetic property, MOF-Fe_3O_4 is synthesized using the Fe_3O_4 core which is notably more significant than the SPIO core of both Au-SPIO and HGNS-SPIO, contributing to the larger mean diameter of MOF-Fe_3O_4 compared to the other two types of MNPs. The TEM measured size for these MNPs are 15 ± 3 nm, 55 ± 11 nm, and 418 nm ± 8 nm for Au-SPIO, HGNS-SPIO, and MOF-Fe_3O_4, respectively. Based on the TEM images, we acknowledge that some nanoparticles, especially MOF-Fe_3O_4, are not perfectly spherical. However, the assumption of a uniform spherical shape for the nanoparticles in our

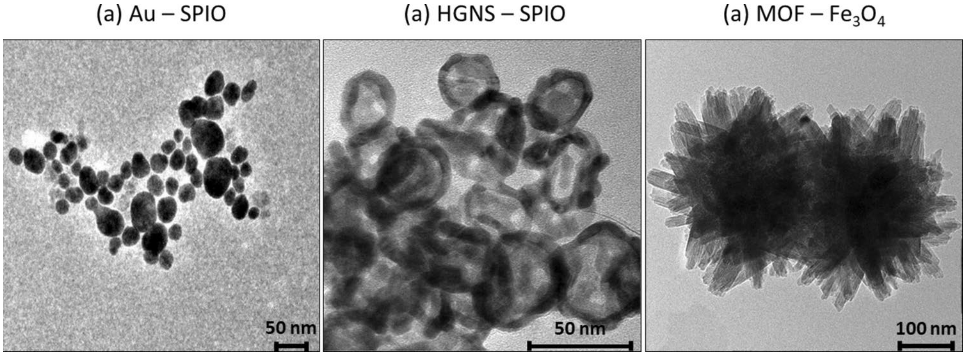

Fig. 6 TEM images of nanosized **a** Au-SPIO, **b** HGNS-SPIO, and **c** MOF-Fe_3O_4

computational fluid dynamics (CFD) model is a practical simplification that reduces computational complexity and allows for more tractable analytical and numerical solutions. Quasi-spherical nanoparticles, like HGNS-SPIO and MOF-Fe3O4, have a shape factor close to that of a perfect sphere, making this approximation reasonable. Although MOF-Fe_3O_4 nanoparticles have a spiky surface, their overall geometry can still be approximated as quasi-spherical. The hydrodynamic behavior of these quasi-spherical nanoparticles can be effectively captured by an equivalent sphere with the same hydrodynamic radius or volume. This simplification allows us to model the average behavior of the nanoparticles in fluid flow accurately. Previous studies have shown that the overall behavior and interactions of spherical and quasi-spherical nanoparticles with biological systems are comparable [44]. Therefore, this assumption is justified for modeling purposes.

The hydrodynamic diameters of these MNPs are 23.6 nm, 115.5 nm, and 406.7 nm for Au-SPIO, HGNS-SPIO, and MOF-Fe_3O_4, respectively (Table 4). The zeta potential of Au-SPIO and HGNS-SPIO are – 42.3 mV and – 30.6 mV, respectively, indicating negatively charged surfaces and confirming repulsion among each other to form a stable suspension in the medium. Meanwhile, the MOF-Fe_3O_4 NP's size is too large, leading to inaccurate determination of a surface charge. Thus, we do not consider them in this measurement.

Table 4 Zeta potential and hydrodynamic diameter measurements

Particle type	Hydrodynamic diameter (nm)	Zeta potential (mV)
Au-SPIO	23.6 ± 0.1	– 42.3 ± 0.8
HGNS-SPIO	115.5 ± 2.1	– 30.6 ± 1.7
MOF-Fe_3O_4	406.7 ± 10.7	Too large, usually inaccurate

This size disparity is noteworthy, as it influences the overall size of the MOF-Fe_3O_4 NPs and underscores the versatility in design achievable with factors affecting their magnetic properties. To explore this, we measured the comparative magnetization hysteresis loops for Au-SPIO and HGNS-SPIO using a vibration sample magnetometer while referring to the literature [27] for MOF-Fe_3O_4. Our decision to use the data from reference [27] was based on the high similarity between the reference sample and our MOF-Fe_3O_4 samples. Our samples and the reference samples have closely matched core–shell thicknesses and overall dimensions, making their magnetic and physical properties highly representative due to the comparable volume of both samples. Illustrated in Fig. 7, the saturation magnetization is 16.23 emu/g, 7.11 emu/g, and 40.23 emu/g for Au-SPIO, HGNS-SPIO, and MOF-Fe_3O_4, respectively—the magnetization curves for the three chosen MNPs exhibited nearly zero coercivity or remanence at room temperature. No discernible hysteresis loop was evident, indicating their typical superparamagnetic behavior [45, 46]. These magnetic characteristics imply that the nanocarriers cannot only be attracted by an external magnet but also ensure no residual magnetism will be retained upon removing the magnetic field.

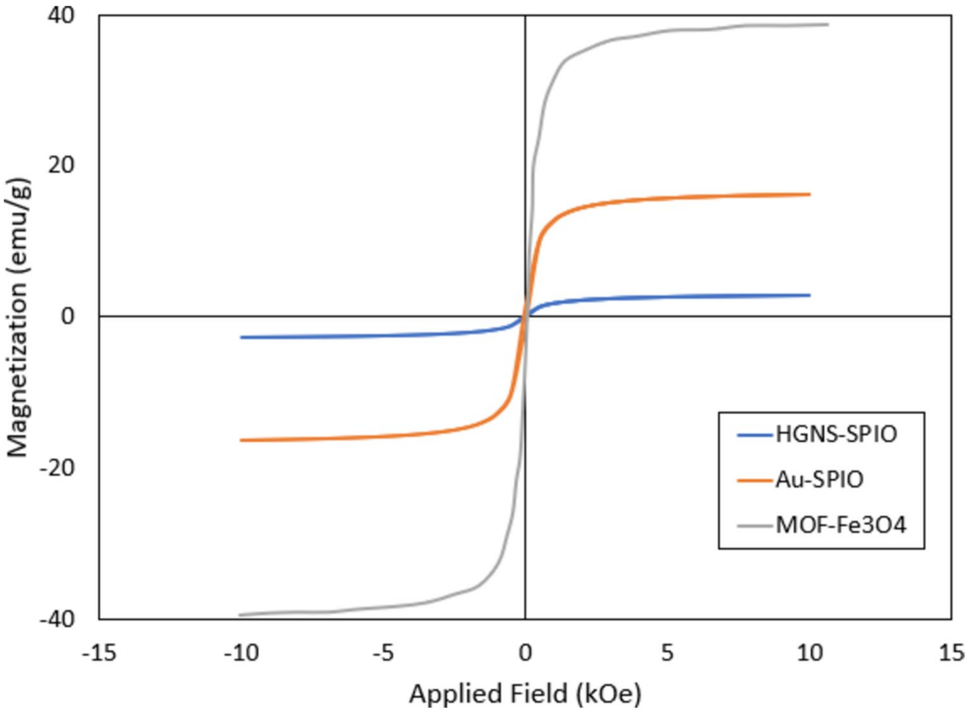

Fig. 7 Magnetization curves from VSM experiment at room temperature for different types of MNPs

5.2 Transport model

Developing an efficient, targeted drug delivery system necessitates exhaustive experimentation and a comprehensive understanding of physiological processes within the human body. The intricate nature of clinical and laboratory studies aimed at optimizing drug delivery systems entails substantial costs, a multitude of experiments, and the utilization of sophisticated instrumentation to accurately assess physical phenomena such as fluid dynamics, particle kinetics, and delivery efficiency. Furthermore, ethical considerations introduce additional challenges. The utilization of CFD-based finite element analysis offers a pathway to scrutinize physiological complexities with heightened precision, reduced economic overheads, and expedited timelines, all while sidestepping ethical dilemmas. In this study, we leveraged CFD-based computational analysis to refine and investigate different targeted brain delivery systems, utilizing patient-specific anatomical geometries. Under thorough analysis, we could determine the ideal type and size of drug-loaded MNPs alongside magnetic configurations to maximize delivery efficiency at distal brain regions.

5.2.1 Fluid flow and magnetic field

The blood flow velocity within the CoW and the external magnetic field profoundly influences the dynamics of MNPs inside the blood flow. Prior research has highlighted the dependence of MNP motion within arteries on factors such as blood flow patterns and the magnitude and orientation of magnetic fields [17, 26, 47]. In this study, the transient simulation of pulsed blood flow was performed within the CoW for 3 s, with each cardiac cycle from $t=0$ s to $t=0.15$ s. The blood flow stream shown in Fig. 8 revealed intricate flow patterns within the brain vasculature, realistically capturing the complexities of blood circulation. The figure depicts the velocity flow field in this patient-specific geometry at three different times in the cardiac cycle from the highest to the lowest inlet flow velocity, with an average velocity of 6.2 mm/s. This agrees well with results reported from literature for the same mice type of C57BL/6 [48]. Notably, the flow velocity increased in the bifurcated areas, and the fluid flow decreased in the narrower branches of CoW. This phenomenon likely stems from the reduction in cross-sectional area downstream, thereby lowering Reynolds numbers, consistent with findings from previous studies [49, 50]. Under consideration of non-Newtonian behaviors and variations in blood viscosity, our model accurately represented curvature, pressure distribution, and shear stress tailored to the patient-specific brain environment. This comprehensive approach enhances our understanding of blood flow dynamics within the CoW while laying a solid foundation for further investigations into MNP transport and delivery mechanisms. The velocity–time correlation provides key insights into blood flow dynamics and nanoparticle delivery. By identifying peak velocities, we can optimize the timing of nanoparticle

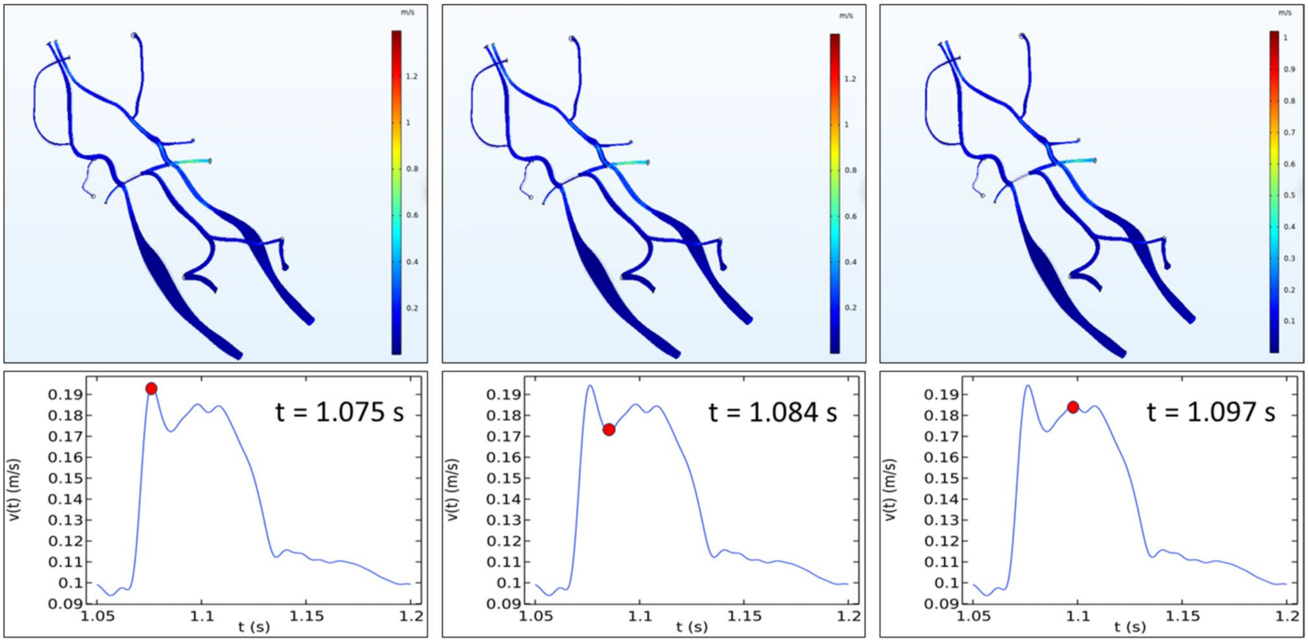

(a) (b) (c)

Fig. 8 The velocity values of blood flow throughout a cardiac cycle and the velocity profile in the simulation domain for CoW, measured in meters per second (m/s). Subfigures show the velocity profile at three specific time points: **a** $t=1.075$ s, **b** $t=1.084$ s, and **c** $t=1.097$ s. The x-axis represents time (s), and the y-axis represents velocity (m/s) administration for maximum distribution and uptake. Higher velocities enhance nanoparticle dispersion throughout the vascular network, making this analysis crucial for improving the effectiveness of targeted drug delivery systems.

On the other hand, the effects of the magnets' size, location, and arrangement were also assessed on the performance of drug delivery in the brain CoW using nanocarriers. Magnetic flux density patterns for three distinct magnetic configurations—a single magnet, linear Halbach array, and circular Halbach array—are illustrated in Fig. 9. As anticipated for permanent magnets, the highest magnetic flux density (B) was observed at the magnet's center, reaching a peak value of $B = 1.23$ Tesla. In contrast, the linear Halbach array demonstrated a more uniform distribution of magnetic flux density along its length. Its maximum value of $B = 2.06$ T. This arrangement may offer coverage and penetration depth advantages within the brain vasculature, facilitating broader targeting capabilities across the CoW. Similarly, the circular Halbach array exhibited a unique magnetic flux density pattern characterized by radial symmetry around its central axis. This configuration may present opportunities for comprehensive and evenly distributed magnetic targeting throughout the CoW, potentially enhancing the uniformity and efficacy of drug delivery to the brain.

5.2.2 MNP transport and distribution

Drawing from the outcomes derived from the calculated blood flow field and external magnetic field, the simulation of MNP distribution within the CoW was investigated. The location and capturing of nanocarriers under non-magnetic field and magnetic field application are depicted in Figs. 10 and 11. Following the pulse blood flow path, most MNPs accumulate at vessel bifurcation or branching sites, where blood flow patterns are disrupted or slower, leading to areas of low shear stress and potential particle entrapment. Regions with complex vascular geometry, such as sharp turns or tortuous segments (left PCA and left MCA), can impede the movement of nanoparticles, leading to their lesser accumulation.

Further details for capture efficiency under different settings are shown in Table 5 for each outlet. In general, the accumulative capture efficiency is around 10.5% for all three types of MNP under non-magnetic field setups,

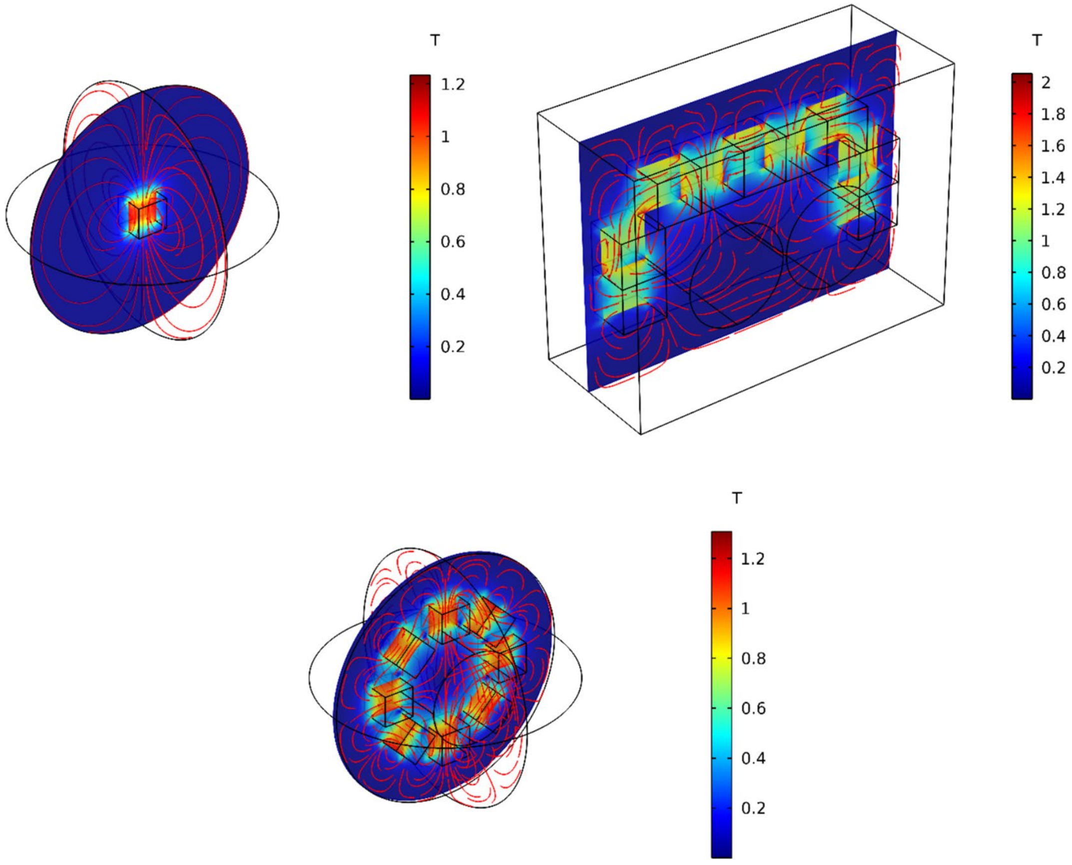

Fig. 9 Magnetic flux density of different calculated magnetic field configurations. Top: (left) single magnet, (right) linear Halbach array. Bottom: circular Halbach array (unit: Tesla)

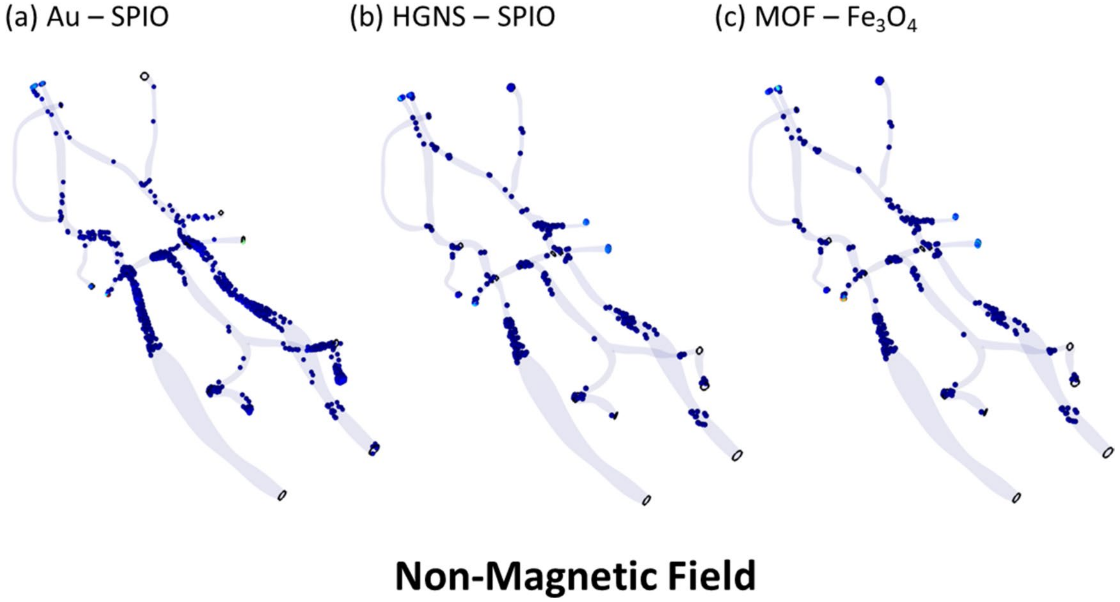

Fig. 10 MNP distribution without magnetic field inside the CoW: **a** Au-SPIO, **b** HGNS-SPIO, **c** MOF-Fe_3O_4

Fig. 11 Particle distribution with linear Halbach array inside the CoW: **a** Au-SPIO, **b** HGNS-SPIO, **c** MOF-Fe_3O_4

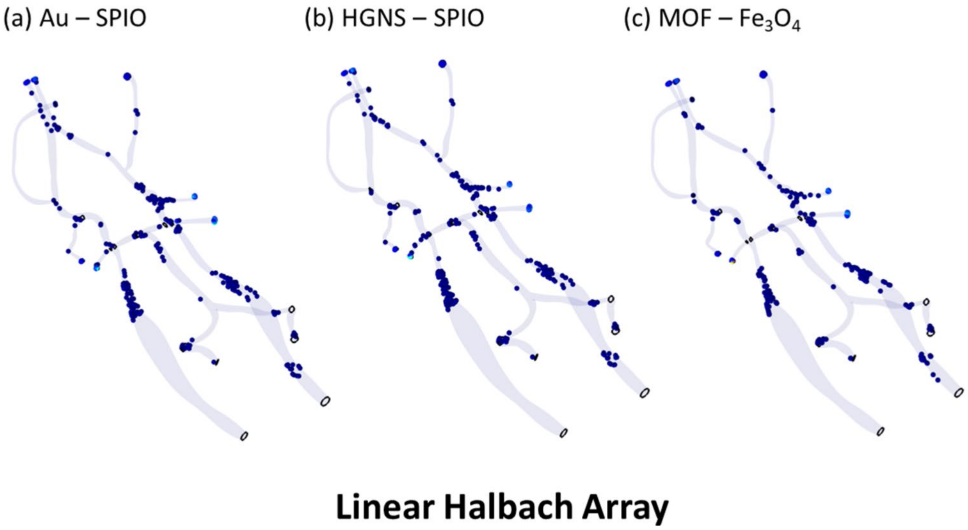

with smaller-size MNPs like Au-SPIO and HGNG-SPIO having slightly higher percentages. This result agrees with data from a reported study by Cooley et al., showing larger particles ranging above 200 nm are harder to transport and have a higher chance of localization and retention at the artery wall in a flow environment [51]. Specifically, without magnetic field application, smaller MNPs exhibit enhanced mobility and can navigate along the blood flow more quickly compared to larger counterparts like MOF-Fe_3O_4. This behavior can be attributed to reduced drag forces experienced by smaller MNPs, allowing them to penetrate deeper into the CoW and reach target sites with greater efficiency. The observed presence of nanoparticles at the inlet after circulation can be explained by their dynamics within the Circle of Willis (CoW) model. The tortuous and branching nature of the CoW creates regions of low velocity and recirculation near the inlet, where nanoparticles can become trapped, preventing them from being fully flushed out with the main flow. The pulsatile flow further influences these dynamics, which may cause nanoparticles to oscillate or settle in these low-flow zones periodically throughout the cardiac cycle. Upon the application of a magnetic field, the capture efficiency shifted positively only for Au-SPIO and MOF-Fe_3O_4, with the percentage increase at most for MOF-Fe_3O_4 in “single magnet” positioning at 0.75%, Au-SPIO in “linear Halbach array” arrangement at 0.34%, and

Table 5 MNPs are distributed in the CoW for different MNPs under different configurations

Outlet	Capture efficiency (%)											
	Non-magnetic field			Single magnet			Linear array			Circular array		
	HGNS-SPIO	MOF-Fe_3O_4	Au-SPIO	HGNS-SPIO	MOF-Fe_3O_4	Au-SPIO	HGNS-SPIO	MOF-Fe_3O_4	Au-SPIO	HGNS-SPIO	MOF-Fe_3O_4	Au-SPIO
L-PCA	0.094	0.094	0.094	0.094	0.063	0.094	0.094	0.125	0.094	0.094	0.094	0.094
R-PCA	0.625	0.625	0.531	0.594	0.750	0.781	0.594	0.938	0.688	0.563	0.844	0.875
L-SCA	0.406	0.406	0.438	0.406	0.500	0.406	0.406	0.344	0.406	0.406	0.375	0.344
R-SCA	2.938	3.063	3.031	3.063	3.125	3.188	3.031	3.000	3.156	3.125	3.094	3.094
L-MCA	0.250	0.219	0.188	0.219	0.250	0.250	0.250	0.125	0.250	0.188	0.188	0.250
R-MCA	1.188	1.188	1.125	1.094	1.313	1.125	1.281	1.375	1.188	1.188	1.281	1.125
L-ACA	2.469	2.375	2.563	2.406	2.625	2.469	2.375	1.938	2.563	2.438	2.281	2.625
R-ACA	2.656	2.469	2.563	2.625	2.563	2.531	2.531	2.875	2.531	2.500	2.750	2.563
Total	10.625	10.438	10.531	10.500	11.188	10.844	10.563	10.719	10.875	10.500	10.906	10.969

MOF-Fe_3O_4 in "circular Halbach array" layout at 0.47%, under identical blood flow field conditions. This can be explained as larger magnetic core/shell ratios endowed with more substantial magnetic properties per MNP, like Au-SPIO and MOF-Fe_3O_4, showcased superior cumulative capturing efficiency across all three magnetic configurations compared to their smaller magnetic core/shell ratio counterpart of HGNS-SPIO with weaker magnetic permeability. The increase of the magnetic field strength intensified the magnetic force acting on these MNPs and the possibility of capturing the MNPs. These findings align with theoretical expectations from Eq. 8, wherein magnetophoretic force escalates proportionally with MNP diameter and magnetic permeability.

It should be noted that, due to the high flow rate, only around 10% of the drug-carrying MNPs are captured by the magnetic applicator due to the domination of the MNP's Stokes drag force. This outcome correlates with prior in vivo findings with the same mice type. Au-SPIO NPs exhibited a delivery efficiency of merely 4.01% to the brain tissue following diffusion from the bloodstream, with a marginal increase of 0.33% observed with a static magnetic field [26].

Our model exhibited distinctive distribution patterns, diverging from other simplified geometry cases, with uneven distributions observed across different outlets. Predominantly, MNP delivery skewed toward the correct SCA at an average of 3.01%, alongside the left and right ACA at 2.47% and 2.56%, respectively. The variations in flow velocity across different CoW regions contribute to heterogeneous MNP distribution patterns, with specific areas experiencing enhanced MNP retention due to reduced flow rates or vessel geometries conducive to MNP trapping.

Moreover, a unique analysis of the bioavailability of MNPs across different brain regions, tailored to various PD stages, was also conducted. By quantifying the accumulative capture efficiency at outlet territories associated with the cerebellum, midbrain, and cortex regions, as shown in Fig. 2, we elucidated the effectiveness of diverse settings across distinct PD stages. The distribution results for brain regions are presented in Table 6 for different magnetic field applications. In the cerebellum, the highest capture efficiency was observed for Au-SPIO under the Circular Array configuration (0.969%), followed by MOF-Fe_3O_4 (0.813%). Conversely, in the midbrain region, MOF-Fe_3O_4 exhibited the highest capture efficiency across many configurations, with the single magnet condition yielding the highest efficiency (1.563%). For the cortex, both Au-SPIO and HGNS-SPIO MNPs displayed the highest capture efficiency, reaching its peak under the non-magnetic field condition (5.125%).

These results were further compared to the animal study [26] conducted in 8-week-old male C57BL/6N mice to evaluate the effect of magnetic field application in the bioavailability of Au-SPIO within the brain (similarly dissected into

Table 6 MNPs distribution in different brain regions for different MNPs under different configurations

Brain region	Capture efficiency (%)											
	Non-magnetic field			Single magnet			Linear array			Circular array		
	HGNS-SPIO	MOF-Fe_3O_4	Au-SPIO	HGNS-SPIO	MOF-Fe_3O_4	Au-SPIO	HGNS-SPIO	MOF-Fe_3O_4	Au-SPIO	HGNS-SPIO	MOF-Fe_3O_4	Au-SPIO
Cerebellum	0.719	0.719	0.625	0.688	0.813	0.875	0.688	1.063	0.781	0.656	0.938	0.969
Midbrain	1.438	1.406	1.313	1.313	1.563	1.375	1.531	1.500	1.438	1.375	1.469	1.375
Cortex	5.125	4.844	5.125	5.031	5.188	5.000	4.906	4.813	5.094	4.938	5.031	5.188

Table 7 Au-SPIO distribution in different brain regions under different magnetic configurations for reported animal study [26]

Brain region	Bioavailability (%)	
	Non-magnetic field	Linear array
Cerebellum	1.52	1.62
Midbrain	1.18	1.37
Cortex	0.98	1.02

midbrain, cortex, and cerebellum regions). The experiment involved the administration of the MNPs via intraperitoneal injection (IP) using Au-SPIO NPs. The parameters of the Au-SPIO nanoparticles, including size and magnetic characteristics, used in our study are similar to those reported in our previous work [26]. This similarity allowed us to use the cited data from [26] to validate our model, ensuring the reliability and accuracy of our simulations. While our previous work focused solely on Au-SPIO, our study expands the scope by comparing three different types of nanoparticles: Au-SPIO, HGNS-SPIO, and MOF-Fe3O_4. This broader comparison aims to evaluate the performance of multiple nanoparticles, highlighting the unique properties and potential advantages of each type for targeted applications. Biodistribution data were calculated by measuring the gold (Au) levels averaged across all time points in the specific brain regions to reflect the concentration of the MNPs (Table 7).

Specifically, our simulation outcomes for Au-SPIO in linear Halbach array configuration compared with non-magnetic field condition presented an increase of 0.156% and 0.125% in capture efficiency for the cerebellum and midbrain, respectively (Table 6). These results closely parallel the same brain regions observed in the animal study, as shown in Table 7, where an increase in bioavailability for the cerebellum and midbrain is 0.1% and 0.19%, respectively, under the impact of the magnetic field. This agreement further validates the efficacy of our simulation model in predicting the effects of magnetic field application on the distribution of MNPs within the brain. However, the increase in capture efficiency is not that significant, suggesting further optimization may be necessary to achieve a more substantial enhancement in delivery performance. Several factors could contribute to this modest improvement overall. Firstly, the inherently complex nature of brain vasculature and blood flow dynamics, such as more significant cross-sectional velocity in narrow artery regions, influence the distribution of MNPs within the brain considerably. Small changes in MNP properties or magnetic field configurations may not always lead to significant alterations in capture efficiency due to the complicated interplay of these factors.

Additionally, the relatively smaller size of the MNPs (weaker magnetic properties) and their interaction with the magnetic field are still weak compared to the magnitude of the drag force. In some cases, the magnetic force exerted on the particles may not be sufficient to substantially alter their distribution within the brain vasculature, resulting in only marginal improvements. From this result, smaller size and lighter but stronger magnetic properties for spherical MNPs are favorable for increasing the bioavailability in the brain to its maximum extent. However, further modeling on different MNP morphologies still needs to be performed to elucidate how other geometrical features impact their interactions with blood flow and capture efficiency.

By performing a comparative study, we have demonstrated that variations in MNP size, composition, and magnetic properties profoundly impact their distribution patterns and targeting efficiency under different settings. Our findings underscore the importance of considering anatomical variations and hemodynamic conditions in MNP delivery optimization. Variations in hemodynamics and flow velocity across various regions of the CoW resulted in heterogeneous MNP distribution patterns, with specific areas exhibiting enhanced MNP capturing. This highlights the complexity of MNP transport within the brain vasculature and emphasizes the need for tailored approaches to maximize therapeutic efficacy while minimizing off-target effects. With the introduction of magnetic fields, the application significantly altered distribution patterns of the targeted delivery, positively increasing efficacy for carriers with larger sizes and magnetic properties. From the clinical applications point of view, the most critical parameter is the local capturing efficiency. This targeted approach offers the potential to overcome the challenges associated with passive diffusion and systemic circulation, thereby improving therapeutic outcomes for neurological disorders. By comparing our simulation results to the findings from these experiments, we demonstrate the model's capability to predict drug distribution in vivo delivery accurately. This alignment between simulation and experimental data highlighted our computational framework's reliability and predictive power in simulating real-world drug delivery scenarios within the brain.

5.3 In vitro biocompatibility analysis of different types of magnetic nanocarriers

The assessment of toxicity and potential side effects of magnetic nanocarriers on the subject body constitutes a crucial aspect in formulating an effective drug delivery system. The toxicity profile of nanocarriers, including Au-SPIO, HGNS-SPIO, and MOF-Fe_3O_4, when utilized as nano-sized drug delivery systems, is contingent upon several factors such as their physicochemical properties, dosage, exposure duration, and the specific target site for delivery. Previous research [52, 53] has indicated that the MOFs and MNPs investigated in this study exhibit low toxicity and favorable biocompatibility. Nonetheless, it remains imperative to fine-tune their dimensions and dosage to minimize potential toxicity while maximizing their efficacy as targeted drug delivery systems.

In vitro investigations assessed the interaction between N2A cells and Au-SPIO, HGNS-SPIO, and MOF-Fe_3O_4, focusing on cellular accumulation and cytocompatibility. The study involved an initial analysis of the morphological changes in N2A cells exposed to each MNP type under different concentrations and durations using a cell-based automated microscope. Comparative analysis with untreated control cells revealed no discernible alterations in the gross structure of the overall morphology of cells exposed to Au-SPIO, HGNS-SPIO, or MOF-Fe_3O_4, as shown in Fig. 12a–c. The shapes and sizes of cells remained within the normal variation range, with no indications of cellular or nuclear abnormalities, membrane-bound vesicles, or cell rupture.

For up to 5 days of incubation, Au-SPIO NPs did not show any sign of toxicity on N2A cell viability at 40 μg/mL compared with the control. Meanwhile, HGNS-SPIO showed a toxicity behavior in a concentration-dependent manner, with cell viability unaffected only at 20 μg/mL concentration (Fig. 13). The enhanced cell viability observed on Day 3 compared to Day 1 in Fig. 14 can be attributed to several factors. One explanation is the adaptation period required by cells to respond to the presence of nanoparticles. Initially, cells might experience a transient stress response due to the introduction of nanoparticles, affecting viability on Day 1. However, as the cells adapt and internalize the nanoparticles, their viability improves, leading to enhanced cell viability by Day 3. Additionally, nanoparticles may promote cell proliferation or provide a more favorable microenvironment for cell growth. Our previous work supported this proliferation effect, demonstrating the promotion of neuroregeneration by nanoparticle-mediated effects [54]. This observation highlights the importance of considering temporal dynamics in evaluating the biocompatibility and therapeutic potential of nanoparticles.

For MOF-Fe_3O_4, the cell viability was stable for all 3 incubation days under all the concentrations (Fig. 14). These results suggest that a high dosage of Au-SPIO and MOF-Fe_3O_4 can affect the subject, while a lower dosage of HGNS-SPIO is favored to reduce possible toxicity effects.

On the other hand, the cellular uptake was evident in treated cells, as seen from the presence of cellular accumulation of Au-SPIO, HGNS-SPIO, and MOF-Fe_3O_4 around N2A cell membranes (Fig. 12a–c). Further quantitative analysis using the ICP-Test revealed a time-dependent increase in the cellular association of the MNPs. Approximately 7300 and 300 accumulated MNPs were observed at 2 h for Au-SPIO and HGNS-SPIO, respectively. The uptake rate exceeded 19,500 and 800 NPs for Au-SPIO and HGNS-SPIO at 4 h, then slowly converged, indicating a progressive accumulation of MNPs over time, as shown in Fig. 15. The result illustrates a significantly higher uptake rate of

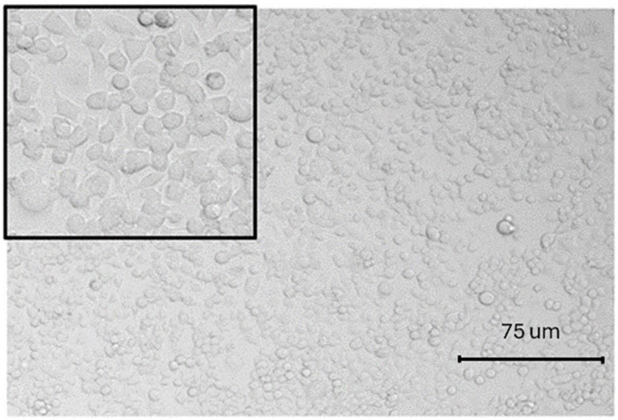

(a) Au – SPIO

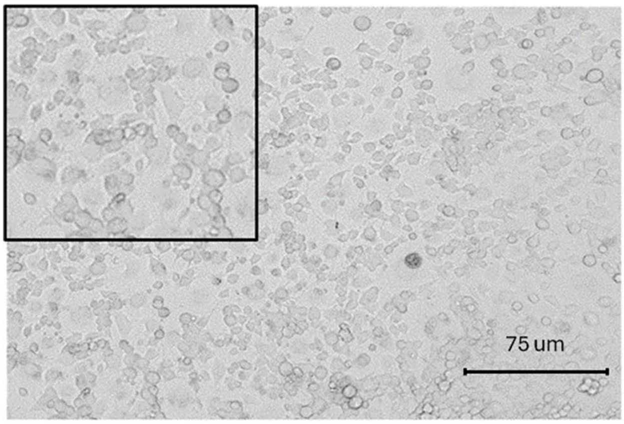

(b) HGNS – SPIO

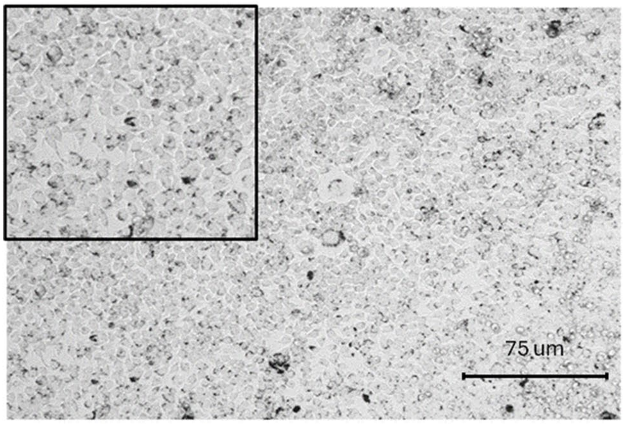

(c) MOF – Fe_3O_4

Fig. 12 The cellular interaction of **a** Au-SPIO, **b** HGNS-SPIO, and **c** MOF-Fe_3O_4 MNPs with Neuro2a cells in the microscopic level for biocompatibility study

Au-SPIO compared to HGNS-SPIO, primarily attributed to the smaller size and uniform spherical shape of Au-SPIO nanoparticles. The smaller size allows Au-SPIO to penetrate cellular membranes through endocytosis mechanisms more easily. Additionally, the uniform spherical shape of Au-SPIO particles promotes efficient interaction with cells, facilitating their internalization. Studies have shown that nanoparticles with smaller sizes and spherical shapes are more readily taken up by cells [55, 56]. These factors collectively enhance the cellular uptake of Au-SPIO nanoparticles compared to HGNS-SPIO, which may have a larger and less uniform shape.

6 Limitation and future direction

While our computational model offers valuable insights into MNP transport within the CoW and the potential of magnetic targeting strategies, we must acknowledge several limitations inherent to our approach. Firstly, our model still represents a reduced-complexity physiological environment of the CoW, neglecting certain anatomical and hemodynamic intricacies that may influence MNP behavior, like the elasticity of vascular wall or blood hematocrit. Additionally, the CoW model we used is simplified and does not include the full complexity of the cerebral vasculature, such as veins, capillaries, and the blood–brain barrier (BBB). Although these simplifications may overlook some critical factors influencing MNP transport and distribution, they allow for a more focused and manageable study of MNP dynamics in a controlled setting. Furthermore, the CoW also exhibits considerable variability across individuals, including variations in vessel geometry, blood flow patterns, and vessel diameters. Our model utilizes patient-specific anatomical geometries but may only partially capture the diversity observed in clinical scenarios.

Secondly, our simulations assume idealized conditions and uniform properties for the MNPs, overlooking potential heterogeneity in MNP size, shape, and surface characteristics. MNP formulations often exhibit polydispersity, influencing their transport and targeting efficiency. Additionally, nanoparticles can form a protein corona during circulation, altering their size, surface properties, and interaction with biological environments.

Thirdly, the blood flow dynamics in the CoW are complex and time-variant, influenced by factors such as patient health conditions, diet, and other physiological parameters, rather than being a steady pulse as assumed in our simulations. Meanwhile, our study acknowledges the potential impact of disease stage, patient age, and gender on the efficacy of nanoparticle-based therapies within the context of the CoW. While our simulation only utilized a standardized MNP concentration based on existing literature and theoretical models, future advancements in personalized medicine could significantly enhance therapeutic outcomes. Tailoring MNP dosing strategies to individual patient profiles could optimize drug delivery efficiency and therapeutic efficacy, considering variations in disease progression, physiological conditions, and patient demographics. It is well-documented that disease stage,

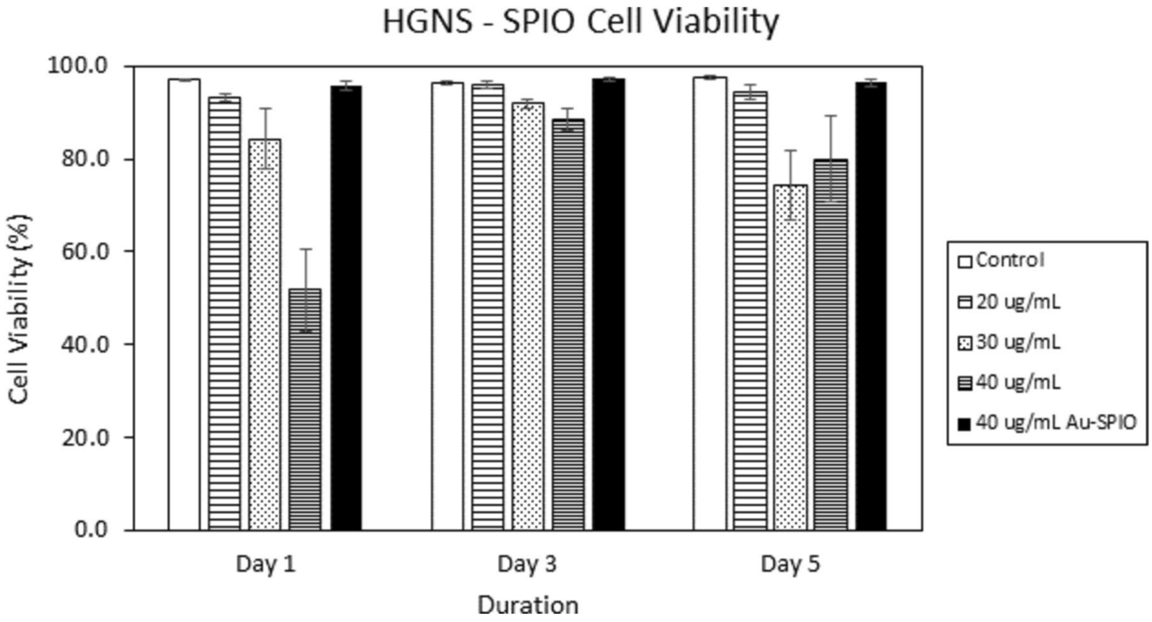

Fig. 13 Cytotoxicity of HGNS-SPIO for in vitro study with Neuro2A determined from flow cytometry. The control group is cells without NPs. $*p<0.05$

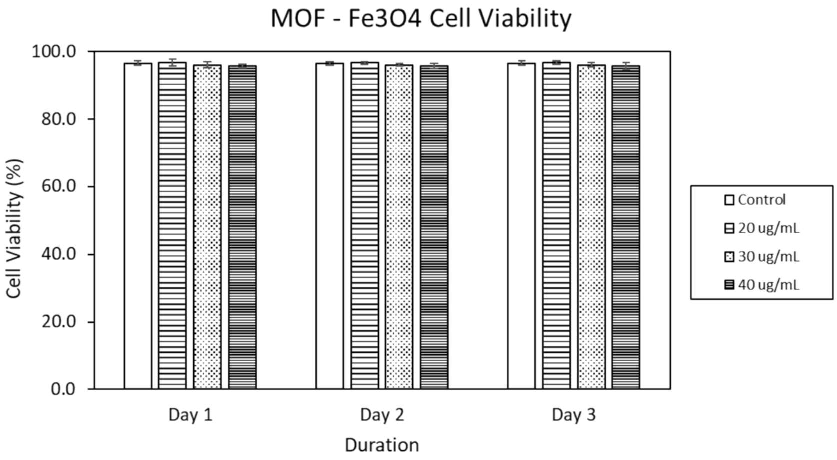

Fig. 14 Cytotoxicity of MOF-Fe_3O_4 for in vitro study with Neuro2A determined from flow cytometry. The control group is cells without MNPs. $*p<0.05$

patient age, and gender can significantly influence nanoparticle pharmacokinetics and biodistribution. For example, studies have shown that nanoparticle clearance rates and tissue distribution can vary with age due to differences in organ function and immune response [57, 58]. Younger individuals typically exhibit more robust immune function and faster metabolic rates, which can lead to quicker clearance of nanoparticles from the bloodstream. Conversely, elderly patients may experience slower clearance rates due to diminished organ function and altered immune responses, leading to prolonged nanoparticle circulation times and different biodistribution profiles. Similarly, gender differences in hormone levels can impact nanoparticle interactions with biological tissues [59]. Hormones such as estrogen and testosterone can influence the permeability of blood vessels and the expression of surface receptors on cells, affecting how nanoparticles are absorbed, distributed, and cleared from the body. Women may experience different nanoparticle biodistribution patterns compared to men due to variations in vascular permeability influenced by hormonal cycles. Furthermore, the disease stage also affects tissue permeability and vascular properties, which in turn influence nanoparticle delivery and retention [60]. In the early stages of certain diseases, the blood–brain barrier (BBB) and other biological barriers may remain relatively intact, restricting nanoparticle penetration. However, as diseases progress, these barriers can become compromised, enhancing nanoparticle delivery and increasing the risk of off-target effects. In conditions such as tumors, the enhanced permeability and

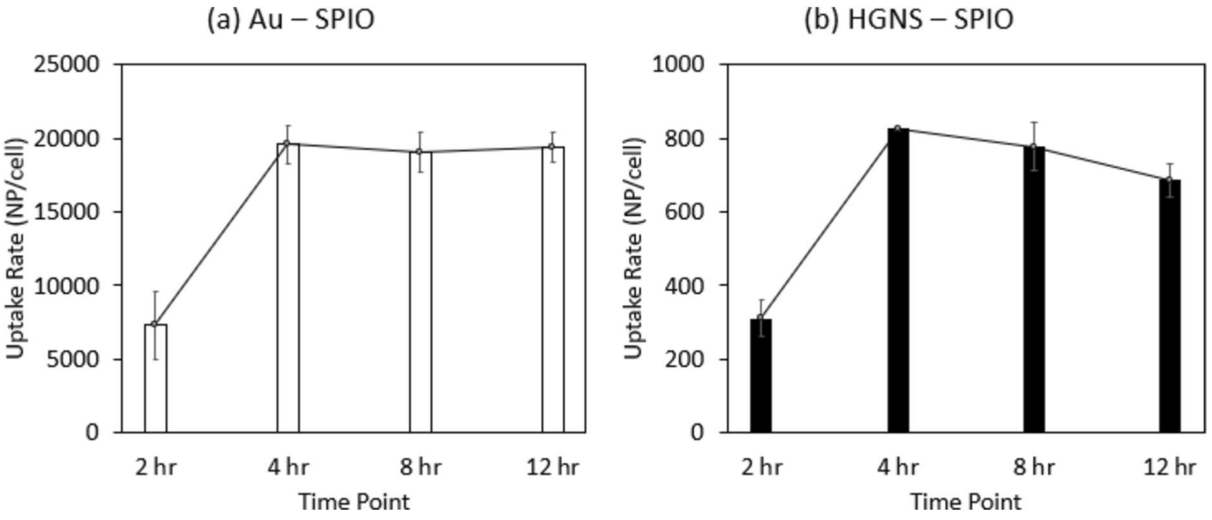

Fig. 15 The cellular uptake rate of Neuro2A cells was measured by elemental analysis for **a** Au-SPIO and **b** HGNS-SPIO

retention (EPR) effect can be more pronounced in later stages, allowing for a more significant accumulation of nanoparticles in the diseased tissue. Conversely, changes in vascular integrity over time can significantly alter the efficacy of nanoparticle-based therapies in chronic conditions like neurodegenerative diseases. Although we did not explore different concentrations in this study, one strength of our model is its ability to predict nanoparticle distribution across various dosages. This feature supports clinicians in developing personalized dosing strategies before conducting extensive in vivo experiments. Further research in this direction is warranted to explore the full potential of customized nanoparticle therapies in neurovascular diseases and beyond.

Lastly, our model focuses primarily on MNP transport within the CoW and does not account for potential clearance mechanisms or biological barriers that MNPs may encounter beyond the vascular system. Clearance mechanisms, such as phagocytosis by immune cells or renal excretion, are crucial in determining MNP biodistribution and pharmacokinetics. While our study provides insights into the potential of magnetic targeting strategies for enhancing MNP delivery to specific brain regions, experimental validation in animal models and clinical studies is necessary to confirm the efficacy and safety of these approaches in vivo. Animal models can provide valuable data on MNP behavior, tissue distribution, and therapeutic outcomes, complementing computational simulations and informing future clinical translation.

7 Conclusion

This study presents a comprehensive investigation into bioengineered MNP transport within the CoW, aiming to elucidate the intricacies of brain-targeted drug delivery. Through diligent characterization and simulation-based analysis, we unveiled crucial insights into the factors governing MNP dynamics, distribution patterns, and targeting efficiency within the complex brain vasculature.

Our characterization results revealed distinctive morphologies and magnetic properties among the synthesized MNPs: Au-SPIO, HGNS-SPIO, and MOF-Fe_3O_4. These variations, including particle size, morphology, and magnetic behavior, significantly influenced their transport dynamics and retention kinetics within the CoW. Smaller NPs exhibited enhanced mobility and penetration capabilities, while larger counterparts demonstrated superior magnetic targeting efficiency. Incorporating patient-specific anatomical data and physiological parameters in our CFD simulations enabled a realistic portrayal of blood flow dynamics, facilitating a nuanced understanding of MNP transport within the CoW. Furthermore, our investigation into magnetic targeting strategies demonstrated the efficacy of external magnetic fields in guiding MNP motion toward specific brain regions. Through systematic analysis of magnetic flux density patterns and MNP distribution profiles, we established the potential of magnetic targeting to enhance spatial specificity and improve drug delivery efficiency within the CoW.

The next phase of our research will focus on addressing the limitations identified in this study and further advancing our understanding of brain-targeted drug delivery. Specifically, we aim to refine our computational model by incorporating additional physiological complexities, such as clearance mechanisms, and the impact of MNP heterogeneity and potential interactions with biological components on their transport dynamics and targeting efficiency. Additionally, we will extend our investigations beyond the CoW to encompass other brain regions and biological barriers to NP biodistribution and pharmacokinetics. This expansion will provide a more comprehensive understanding of MNP behavior in vivo in subsequent animal models to validate the model. These experiments will complement our computational simulations and provide essential data for informing future clinical translation.

Our findings underscore the significance of personalized medicine approaches and computational modeling in optimizing brain-targeted drug delivery systems. By elucidating the interplay between MNP properties, fluid dynamics, and magnetic fields, our model serves as a drug carrier prescreening tool to provide valuable insights for designing and optimizing therapeutic interventions for neurological disorders. This enhanced understanding holds promise for developing more effective, targeted, and personalized treatments, ultimately improving patient outcomes and quality of life.

Supplementary Information The online version contains supplementary material available at https://doi.org/10.1007/s42114-024-01013-2.

Acknowledgements We acknowledge the financial support from the United States National Science Foundation (NSF) (CAREER Award # CMMI 1851635, Y.W. and GCR awards # ECCS 2021081 (Y.W.)). We would also like to acknowledge the Elemental Analysis Lab at the Chemistry Department of Texas A&M University for performing ICP-MS analysis in this study.

Author contribution The manuscript was written through the contributions of all authors. Nguyen Nguyen performed the computational simulations. Nguyen Nguyen, Hanwen Hu, Tian-Hao Yan, Tianzhu Fan, and Muzhaozi Yuan performed material preparation, characterization, and result analysis. In vitro cell work was performed by Nguyen Nguyen and Zhifeng Xiao. Nguyen Nguyen and Muzhaozi Yuan prepared the initial draft of the manuscript. Hong-Cai Zhou, Jean-Philippe Pellois, Ying Li, and Ya Wang reviewed and revised previous manuscript versions. All authors have read and approved the final version of the manuscript.

Funding We would like to thank the financial support from the United States National Science Foundation (NSF) (CAREER Award # CMMI 1851635, Y.W. and GCR awards # ECCS 2021081 (Y.W.)). This work was also supported by the award R01GM110137 (J.-P.P.) from the US National Institute of General Medical Sciences.

Data availability The data that support the findings of this study are not openly available due to reasons of sensitivity and are available from the corresponding authors upon reasonable request.

Declarations

Competing interests The authors declare no competing interests.

References

1. Van Schependom J, D'Haeseleer M (2023) Advances in neurodegenerative diseases. J Clin Med 12:1709
2. Naik N, Adeyanju O, Samrot AV, Bhat P, Salmataj SA (2023) Drug delivery through microneedles for improved permeability and efficacy: fabrication, methodology and applications. Eng Sci 26:1065
3. Bahaar H, Reddy SG, Kumar BS, Prashanthi K, Murthy HCA (2023) Modified layered double hydroxide–PEG magneto-sensitive hydrogels with suitable ligno-alginate green polymer composite for prolonged drug delivery applications. Eng Sci 24:914
4. Bhardwaj AK, Kant A, Rehalia A, Singh V, Sharma R (2023) A review on nanomaterials for drug delivery systems and application of carbon based nanomaterials. ES Mater Manuf 21:824
5. Rahaman SJ, Samanta A, Mir MH, Dutta B (2022) Metal-organic frameworks (MOFs): a promising candidate for stimuli-responsive drug delivery. ES Mater Manuf 19:792
6. Liu H-L, Hua M-Y, Yang H-W, Huang C-Y, Chu P-C, Wu J-S, Tseng I-C, Wang J-J, Yen T-C, Chen P-Y, Wei K-C (2010) Magnetic resonance monitoring of focused ultrasound/magnetic nanoparticle targeting delivery of therapeutic agents to the brain. Proc Natl Acad Sci 107:15205–15210
7. Moghimi SM, Hunter AC, Murray JC (2001) Long-circulating and target-specific nanoparticles: theory to practice. Pharmacol Rev 53:283–318
8. Ruan S, Zhou Y, Jiang X, Gao H (2021) Rethinking CRITID Procedure of brain targeting drug delivery: circulation, blood brain barrier recognition, intracellular transport, diseased cell targeting, internalization, and drug release. Adv Sci 8:2004025
9. Kong SD, Lee J, Ramachandran S, Eliceiri BP, Shubayev VI, Lal R, Jin S (2012) Magnetic targeting of nanoparticles across the intact blood–brain barrier. J Control Release 164:49–57
10. Thomsen LB, Thomsen MS, Moos T (2015) Targeted drug delivery to the brain using magnetic nanoparticles. Ther Deliv 6:1145–1155
11. Busquets M, Espargaró A, Sabaté R, Estelrich J (2015) Magnetic nanoparticles cross the blood-brain barrier: when physics rises to a challenge. Nanomaterials 5:2231–2248

12 Tartaj P, Morales MADP, Veintemillas-Verdaguer S, Gonz Lez-Carre o T, Serna CJ (2003) The preparation of magnetic nanoparticles for applications in biomedicine. J Phys D: Appl Phys 36:R182–R197

13. Gupta AK, Gupta M (2005) Synthesis and surface engineering of iron oxide nanoparticles for biomedical applications. Biomaterials 26:3995–4021
14. Kloster M, de Almeida AA, Muraca D, Marcovich NE, Mosiewicki MA (2023) Chitosan-based magnetic particles as adsorbents for anionic contaminants. Eng Sci 22:851
15. Kim JS, Yoon T-J, Yu KN, Kim BG, Park SJ, Kim HW, Lee KH, Park SB, Lee J-K, Cho MH (2006) Toxicity and tissue distribution of magnetic nanoparticles in mice. Toxicol Sci 89:338–347
16. Nichols JW, Sakurai Y, Harashima H, Bae YH (2017) Nano-sized drug carriers: extravasation, intratumoral distribution, and their modeling. J Control Release 267:31–46
17. Lunnoo T, Puangmali T (2015) Capture efficiency of biocompatible magnetic nanoparticles in arterial flow: a computer simulation for magnetic drug targeting. Nanoscale Res Lett 10:426
18. Kosari E, Vafai K (2021) Transport and dynamic analysis of magnetic nanoparticles in brain microvascular vessels. Phys Fluids 33:081907
19. Hewlin RL, Tindall JM (2023) Computational assessment of magnetic nanoparticle targeting efficiency in a simplified Circle of Willis arterial model. Int J Mol Sci 24:2545
20. Tehrani MD, Yoon JH, Kim MO, Yoon J (2015) A novel scheme for nanoparticle steering in blood vessels using a functionalized magnetic field. IEEE Trans Biomed Eng 62:303–313
21. Kenjereš S, Righolt BW (2012) Simulations of magnetic capturing of drug carriers in the brain vascular system. Int J Heat Fluid Flow 35:68–75
22. Chen J, Wang Y (2020) Personalized dynamic transport of magnetic nanorobots inside the brain vasculature. Nanotechnology 31:495706

23. Tyfa Z, Obidowski D, Reorowicz P, Stefańczyk L, Fortuniak J, Jóźwik K (2018) Numerical simulations of the pulsatile blood flow in the different types of arterial fenestrations: Comparable analysis of multiple vascular geometries. Biocybernetics Biomed Eng 38:228–242
24. Rispoli VC, Nielsen JF, Nayak KS, Carvalho JLA (2015) Computational fluid dynamics simulations of blood flow regularized by 3D phase contrast MRI. Biomed Eng Online 14:1–23
25. Liu H, Lan L, Abrigo J, Ip HL, Soo Y, Zheng D, Wong KS, Wang D, Shi L, Leung TW (2021) Comparison of Newtonian and non-Newtonian fluid models in blood flow simulation in patients with intracranial arterial stenosis. Front Physiol 12:718540
26. Chen J, Yuan M, Madison CA, Eitan S, Wang Y (2022) Blood-brain barrier crossing using magnetic stimulated nanoparticles. J Control Release 345:557–571
27. Xie H (2019) Enzymatic production of biodiesel using immobilized lipase on core-shell structured Fe3O4@MIL-100(Fe) composites. Catalysts 9:850
28. Saito S, Sawada K, Mori Y, Yoshioka Y, Murase K (2015) Brain and arterial abnormalities following prenatal X-ray irradiation in mice assessed by magnetic resonance imaging and angiography. Congenit Anom 55:103–106
29. Chang Y (2019) Improving the Otsu method for MRA image vessel extraction via resampling and ensemble learning. Healthc Technol Lett 6:115–120
30. Hossain SS, Zhang Y, Fu X, Brunner G, Singh J, Hughes TJR, Shah D, Decuzzi P (2015) Magnetic resonance imaging-based computational modelling of blood flow and nanomedicine deposition in patients with peripheral arterial disease. J R Soc Interface 12:20150001
31. Everett NB, Simmons B, Lasher EP (1956) Distribution of blood (Fe59) and plasma (I131) volumes of rats determined by liquid nitrogen freezing. Circ Res 4:419–424
32. Riches AC, Sharp JG, Thomas DB, Smith SV (1973) Blood volume determination in the mouse. J Physiol 228:279–284
33. Yasuda KY, Armstrong RC, Cohen RE (1981) Shear flow properties of concentrated solutions of linear and star branched polystyrenes. Rheol Acta 20:163–178
34. Bernabeu MO, Jones ML, Nielsen JH, Krüger T, Nash RW, Groen D, Schmieschek S, Hetherington J, Gerhardt H, Franco CA, Coveney PV (2014) Computer simulations reveal complex distribution of haemodynamic forces in a mouse retina model of angiogenesis. J R Soc Interface 11:20140543
35. Furlani EP (2010) Magnetic biotransport: analysis and applications. Materials 3:2412–2446
36. Gerber R, Takayasu M, Friedlaender F (1983) Generalization of HGMS theory: the capture of ultra-fine particles. IEEE Trans Magn 19:2115–2117
37. Ranjbar H, Farajollahi A, Rostami M (2023) Targeted drug delivery in pulmonary therapy based on adhesion and transmission of nanocarriers designed with a metal–organic framework. Biomech Model Mechanobiol 22:2153–2170
38. Rietdijk CD, Perez-Pardo P, Garssen J, Van Wezel RJA, Kraneveld AD (2017) Exploring Braak's hypothesis of Parkinson's disease. Front Neurol 8:37
39. Alishiri M, Ebrahimi S, Shamloo A, Boroumand A, Mofrad MRK (2021) Drug delivery and adhesion of magnetic nanoparticles coated nanoliposomes and microbubbles to atherosclerotic plaques under magnetic and ultrasound fields. Eng Appl Comput Fluid Mech 15:1703–1725
40. COMSOL AB (2012) COMSOL Multiphysics Reference Guide (Version 4.3). Stockholm
41. Owen J, Rademeyer P, Chung D, Cheng Q, Holroyd D, Coussios C, Friend P, Pankhurst QA, Stride E (2015) Magnetic targeting of microbubbles against physiologically relevant flow conditions. Interface Focus 5:20150001
42. Feintuch A, Ruengsakulrach P, Lin A, Zhang J, Zhou Y-Q, Bishop J, Davidson L, Courtman D, Foster FS, Steinman DA (2007) Hemodynamics in the mouse aortic arch as assessed by MRI, ultrasound, and numerical modeling. Am J Physiol-Heart Circ Physiol 292:H884–H892
43. De Wilde D, Trachet B, De Meyer G, Segers P (2016) The influence of anesthesia and fluid–structure interaction on simulated shear stress patterns in the carotid bifurcation of mice. J Biomech 49:2741–2747
44. Puchkova LV, Sankova TP, Magazenkova DN, Skomorokhova EA, Orlov IA, Sakhenberg EI, Sosnin IM, Al Farroukh M, Romanov AE, Ilyechova EY (2022) Shape-dependent biological activity of spherical and quasi-spherical silver nanoparticles in E. coli, A549 cells and mice. Environ Sci: Nano 9:3581–3598
45. Yuan M, Feng X, Yan T-H, Chen J, Ma X, Cunha P, Lan S, Li Y, Zhou H-C, Wang Y (2022) Superparamagnetic iron oxide-enclosed hollow gold nanostructure with tunable surface plasmon resonances to promote near-infrared photothermal conversion. Adv Compos Hybrid Mater 5:2387–2398
46. Netto CGCM, Toma HE, Andrade LH (2013) Superparamagnetic nanoparticles as versatile carriers and supporting materials for enzymes. J Mol Catal B: Enzym 85:71–92
47. Mohammadi S, Rafii-Tabar H, Sasanpour P (2022) Contribution of the dipole–dipole interaction to targeting efficiency of magnetite nanoparticles inside the blood vessel: A computational modeling analysis with different magnet geometries. Phys Fluids 34:033601. https://doi.org/10.1063/5.0082882
48. Crouch AC, Cao AA, Scheven UM, Greve JM (2020) In vivo MRI assessment of blood flow in arteries and veins from head-to-toe across age and sex in C57BL/6 mice. Ann Biomed Eng 48:329–341
49. Chaudhry R, Miao JH, Rehman A (2022) Physiology, cardiovascular. In: StatPearls [Internet]. StatPearls Publishing
50. Ebrahimi S, Shamloo A, Alishiri M, Mofrad YM, Akherati F (2021) Targeted pulmonary drug delivery in coronavirus disease (COVID-19) therapy: a patient-specific in silico study based on magnetic nanoparticles-coated microcarriers adhesion. Int J Pharm 609:121133
51. Cooley M, Sarode A, Hoore M, Fedosov DA, Mitragotri S, Gupta AS (2018) Influence of particle size and shape on their margination and wall-adhesion: implications in drug delivery vehicle design across nano-to-micro scale. Nanoscale 10:15350–15364
52. Zhu Z, Jiang S, Liu Y, Gao X, Hu S, Zhang X, Huang C, Wan Q, Wang J, Pei X (2020) Micro or nano: evaluation of biosafety and biopotency of magnesium metal organic framework-74 with different particle sizes. Nano Res 13:511–526
53. Yan T-H, Yuan M, Nguyen N, Chen J, Feng X, Fan T, Harnett MC, Xiao Z, Li Y, Pellois J-P (2023) Surface-modified gold-coated superparamagnetic iron oxide nanoparticles promoting light-controlled drug release. Adv Compos Hybrid Mater 6:226
54. Yuan M, Wang Y, Qin Y-X (2018) Promoting neuroregeneration by applying dynamic magnetic fields to a novel nanomedicine: superparamagnetic iron oxide (SPIO)-gold nanoparticles bounded with nerve growth factor (NGF), Nanomedicine: Nanotechnology. Biol Med 14:1337–1347
55. Augustine R, Hasan A, Primavera R, Wilson RJ, Thakor AS, Kevadiya BD (2020) Cellular uptake and retention of nanoparticles: insights on particle properties and interaction with cellular components. Mater Today Commun 25:101692
56. Zhang S, Li J, Lykotrafitis G, Bao G, Suresh S (2009) Size-dependent endocytosis of nanoparticles. Adv Mater (Deerfield Beach, Fla.) 21:419
57. Alexis F, Pridgen E, Molnar LK, Farokhzad OC (2008) Factors affecting the clearance and biodistribution of polymeric nanoparticles. Mol Pharm 5:505–515

58. Liu W, Wang X, Chen R, Zhang K, Li Y, Li Y, Si D, Gong J, Yin D, Wang Y (2016) Effect of age on the pharmacokinetics of polymorphic nimodipine in rats after oral administration. Acta Pharmaceutica Sinica B 6:468–474
59. Hajipour MJ, Aghaverdi H, Serpooshan V, Vali H, Sheibani S, Mahmoudi M (2021) Sex as an important factor in nanomedicine. Nat Commun 12:2984
60. Natfji AA, Ravishankar D, Osborn HMI, Greco F (2017) Parameters affecting the enhanced permeability and retention effect: the need for patient selection. J Pharm Sci 106:3179–3187